



## In Situ and Satellite-based Estimates of Cloud Properties and Aerosol-Cloud Interactions over the Southeast Atlantic Ocean

Siddhant Gupta<sup>1, 2\*</sup>, Greg M. McFarquhar<sup>1, 2</sup>, Joseph R. O'Brien<sup>3#</sup>, Michael R. Poellot<sup>3</sup>, David J. Delene<sup>3</sup>, Ian Chang<sup>2</sup>, Lan Gao<sup>2</sup>, Feng Xu<sup>2</sup>, and Jens Redemann<sup>2</sup>

5 <sup>1</sup>Cooperative Institute for Severe and High-Impact Weather Research and Operations, University of Oklahoma, Norman, OK, USA

<sup>2</sup>School of Meteorology, University of Oklahoma, Norman, OK, USA

<sup>3</sup>Department of Atmospheric Sciences, University of North Dakota, Grand Forks, ND, USA

10 Now at: \*Brookhaven National Laboratory, Upton, NY, USA and #Argonne National Laboratory, Lemont, IL, USA

*Correspondence to:* Siddhant Gupta ([sgupta@bnl.gov](mailto:sgupta@bnl.gov))

**Abstract.** In situ cloud probe data from the NASA Observations of Aerosols above Clouds and their interactions (ORACLES) field campaign were used to estimate effective radius ( $R_e$ ), cloud optical thickness ( $\tau$ ), and cloud droplet concentration ( $N_c$ ) for marine stratocumulus over the  
15 southeast Atlantic Ocean. The in situ  $R_e$ ,  $\tau$ , and  $N_c$  were compared with co-located Moderate Resolution Imaging Spectroradiometer (MODIS) retrievals of  $R_e$  and  $\tau$ , and MODIS derived  $N_c$ . For  
145 cloud profiles, a MODIS retrieval was co-located with in situ data with a time gap of less than  
1 hour. On average, the MODIS  $R_e$  and  $\tau$  (11.3  $\mu\text{m}$  and 11.7) were 1.6  $\mu\text{m}$  and 2.3 higher than the  
in situ  $R_e$  and  $\tau$  with Pearson's correlation coefficient ( $R$ ) of 0.77 and 0.73, respectively. The  
20 average MODIS  $N_c$  (151.5  $\text{cm}^{-3}$ ) was within 1  $\text{cm}^{-3}$  of the average in situ  $N_c$  with  $R$  of 0.90.

The 145 cloud profiles were classified into 67 contact profiles where aerosol concentration ( $N_a$ ) greater than 500  $\text{cm}^{-3}$  was sampled within 100 m above cloud tops and 78 separated profiles where  $N_a$  less than 500  $\text{cm}^{-3}$  was sampled up to 100 m above cloud tops. Contact profiles had higher in situ  $N_c$  (by 88  $\text{cm}^{-3}$ ), higher  $\tau$  (by 2.5) and lower in situ  $R_e$  (by 2.2



25  $\mu\text{m}$ ) compared to separated profiles. These differences were associated with aerosol-cloud interactions (ACI) and MODIS estimates of the differences were within  $5\text{ cm}^{-3}$ , 0.5, and  $0.2\ \mu\text{m}$  of the in situ estimates when profiles with MODIS  $R_e > 15\ \mu\text{m}$  or MODIS  $\tau > 25$  were removed. The agreement between MODIS and in situ estimates of changes in  $R_e$ ,  $\tau$ , and  $N_c$  associated with ACI was driven by low biases in MODIS retrievals of cloud properties across different aerosol regimes.

30 Thus, when combined with estimates of aerosol location and concentration, MODIS retrievals of marine stratocumulus cloud properties over the southeast Atlantic can be used to study ACI over larger domains and longer timescales than possible using in situ data.

## 1 Introduction

Uncertainties in the effective radiative forcing due to aerosol-cloud interactions (ACI) lead to variability in climate model estimates of Earth's energy budget in future climate scenarios (e.g., Boucher et al., 2013). The ACI for warm, low-level clouds are particularly important due to their dominating impact on the aerosol indirect forcing (Christensen et al., 2016). Further, the shortwave cloud radiative forcing of  $-17.1\ \text{W m}^{-2}$  (Loeb et al., 2009) is largely driven by the ubiquitous low-level clouds (Hartmann et al., 1992). Marine stratocumulus is the most common

40 type of low-level cloud with an annual mean coverage of 23 % of Earth's ocean surface (Wood, 2012). The radiative forcing due to well-mixed greenhouse gases ( $+2.83\ \text{W m}^{-2}$ ) (Myhre et al., 2013) or the doubling of  $\text{CO}_2$  concentration (about  $+2.5\ \text{W m}^{-2}$ ) could be offset by the radiative forcing from just a 15 to 20 % reduction in droplet sizes for low clouds (Slingo, 1990). Low-level clouds are thus strong modulators of planetary albedo and global climate.



45 ACI lead to changes in the cloud radiative forcing through processes that impact cloud  
extinction ( $\beta$ ) and optical thickness ( $\tau$ ) which are closely related to microphysical properties like  
cloud droplet concentration ( $N_c$ ), effective radius ( $R_e$ ), and liquid water content (LWC). Cloud  
radiative forcing is a strong function of  $R_e$ , which represents the mean droplet size retrieved from  
radiative transfer calculations (Hansen and Travis, 1974). An increase in aerosol concentration  
50 ( $N_a$ ) can increase the number of cloud condensation nuclei and lead to higher  $N_c$  and lower  $R_e$   
when LWC remains constant. These aerosol-induced changes in  $N_c$  and  $R_e$  lead to clouds with  
higher reflectance or  $\tau$  which results in an indirect radiative forcing (Twomey, 1974; 1977).  
However, ACI are often masked by meteorological conditions (Mauger and Norris, 2007) and  
other cloud responses to increasing  $N_a$  like invigoration (Douglas and L'Ecuyer, 2021).  
55 Uncertainties in estimating the impact of ACI on cloud albedo are also driven by differences  
between process scales for ACI and the resolution of climate models or satellite retrievals  
(McComiskey and Feingold, 2012). The inconsistency in ACI estimates due to the scale differences  
is addressed by combining satellite retrievals with airborne observations for specific regimes.

A regime of interest for ACI exists over the southeast Atlantic Ocean where an extensive  
60 stratocumulus deck is overlaid by biomass burning aerosols from southern Africa (Haywood et  
al., 2004; Adebisi and Zuidema, 2016). The biomass burning aerosols exert a direct radiative  
forcing by absorbing solar radiation (Cochrane et al., 2019) and heating due to the aerosol  
absorption can impact atmospheric stability (Cochrane et al., 2022). Changes in the  
thermodynamic profile can lead to changes in cloud properties and result in a semi-direct forcing  
65 (Johnson et al., 2004; McFarquhar and Wang, 2006; Wilcox, 2010). Climate models struggle to  
simulate these radiative effects and the altitude of the above-cloud aerosol layer over the



southeast Atlantic leading to biases in model estimates of low-cloud feedbacks and ACI (Das et al., 2020; Mallet et al., 2021).

Airborne campaigns have been conducted over the southeast Atlantic since 2016 to  
70 understand the ACI in this region and their impact on global climate (Zuidema et al., 2016;  
Formenti et al., 2019; Haywood et al., 2021). During the NASA ObseRvations of Aerosols above  
CLouds and their intEractionS (ORACLES) field campaign (Redemann et al., 2021), in situ  
measurements of cloud droplet size distributions, from which  $N_c$ ,  $R_e$ , and  $\tau$  can be estimated,  
were collected over the southeast Atlantic at locations with contact or separation between the  
75 base of the aerosol layer and stratocumulus cloud tops. Variable vertical separation between the  
aerosol and cloud layers was associated with aerosol-induced changes in  $N_c$ ,  $R_e$ , and  $\tau$  (Gupta et  
al., 2021, hereafter G21) and precipitation suppression (Gupta et al., 2022, hereafter G22).  
Satellite retrievals of  $N_c$ ,  $R_e$ , and  $\tau$ , and aerosol-induced changes in  $N_c$ ,  $R_e$ , and  $\tau$  could enable such  
investigations of ACI over larger domains and longer timescales than in situ measurements.

80 The Earth Observing System Terra and Aqua satellites provide global coverage of cloud  
microphysical properties using the Moderate Resolution Imaging Spectroradiometer (MODIS).  
MODIS acquires data for 36 atmospheric bands from 0.4  $\mu\text{m}$  to 14.4  $\mu\text{m}$  including a non-  
absorbing band (0.86  $\mu\text{m}$  over ocean) which provides information on  $\tau$  and a water absorbing  
band (1.6, 2.1, or 3.7  $\mu\text{m}$ ) which provides information on  $R_e$  (Platnick et al., 2003). Reflectance  
85 pairs from these bands allow simultaneous retrievals of  $R_e$  and  $\tau$  (Nakajima and King, 1990). In  
the absence of direct retrievals, MODIS  $N_c$  can be estimated assuming adiabatic LWC (Breguier  
et al., 2000; Szczodrak et al., 2001). However, MODIS retrievals of cloud properties have biases



relative to in situ  $N_c$ ,  $R_e$ , and  $\tau$  depending on the cloud type and sampling strategy (Gryspeerd et al., 2021; Fu et al., 2022), occurrence of drizzle (Zinner et al., 2010), width and shape of droplet  
90 size distributions (Chang and Li, 2002; Brenguier et al., 2011), vertical profile of  $R_e$  (McFarquhar and Heymsfield, 1998; Platnick, 2000), and cloud adiabaticity (Min et al., 2012; Merk et al., 2016; Braun et al., 2018). Results from comparisons of MODIS retrievals with in situ data also depend on the cloud probes used for in situ measurements (King et al., 2013; Witte et al., 2018) and the co-location of the MODIS and in situ datasets (Painemal and Zuidema, 2011, hereafter PZ11).

95 A review of satellite-based estimates of  $N_c$  concluded that airborne datasets are underutilized for satellite retrieval evaluation (Grosvenor et al., 2018). This study compares in situ  $N_c$ ,  $R_e$ , and  $\tau$  from ORACLES with MODIS retrievals of  $R_e$  and  $\tau$  (Platnick et al., 2017a) and the MODIS derived  $N_c$  based on the assumption of adiabatic LWC. Previous work comparing MODIS retrievals with in situ observations of marine stratocumulus (PZ11; Min et al., 2012; Noble and Hudson,  
100 2015; Braun et al., 2018; Witte et al., 2018) was extended by using a larger in situ dataset which provides cloud and aerosol measurements under conditions of variable vertical separation between the aerosol and cloud layers. Biases in MODIS retrievals of cloud properties are quantified as a function of the time gap between MODIS retrievals and in situ data. Biases in MODIS Aqua are compared with biases in MODIS Terra and MODIS and in situ estimates of  
105 aerosol-induced changes in  $N_c$ ,  $R_e$ , and  $\tau$  are compared.

The paper is organized as follows. In situ observations and satellite retrievals used in the study are described in Section 2 along with the methodology for spatiotemporal co-location of the in situ and satellite datasets. In Section 3, the MODIS  $R_e$ ,  $\tau$ , and  $N_c$  are compared with in situ



$R_e$ ,  $\tau$ , and  $N_c$ , potential sources of biases are discussed, and uncertainties and errors are  
110 quantified. In Section 4, MODIS estimates of aerosol-induced changes in  $R_e$ ,  $\tau$ , and  $N_c$  over the  
southeast Atlantic are compared with in situ estimates. Implications for studies of ACI over the  
southeast Atlantic are discussed in Section 5. The conclusions are presented in Section 6.

## 2 Data and Methodology

### 2.1 In situ Observations

115 In situ observations of marine stratocumulus over the southeast Atlantic were collected  
during ORACLES using the NASA P-3B aircraft (Redemann et al., 2021). In situ cloud sampling was  
conducted during vertical profiles through the stratocumulus layer (hereafter, cloud profiles)  
between 10° W to 15° E and 5° N to 20° S in September 2016, August 2017, and October 2018  
(G22). For each cloud profile, data from in situ cloud probes were used to derive the number  
120 distribution function ( $n(D)$ ) for droplets with diameter ( $D$ ) between 3 to 19200  $\mu\text{m}$ . The cloud  
probes used during ORACLES included a Cloud and Aerosol Spectrometer (CAS) (Baumgardner et  
al., 2001), three Cloud Droplet Probes (CDPs) (Lance et al., 2010), a Two-Dimensional Stereo  
probe (2D-S) (Lawson et al., 2006), a Phase Doppler Interferometer (PDI) (Chuang et al., 2008),  
and a High Volume Precipitation Sampler (HVPS-3) (Lawson et al., 1998). A King hot-wire probe  
125 (King et al., 1978) measured LWC (hereafter, King LWC). A Passive Cavity Aerosol Spectrometer  
Probe (PCASP) (Cai et al., 2013) measured  $n(D)$  for accumulation-mode aerosols ( $0.1 < D < 3 \mu\text{m}$ ).

The Airborne Data Processing and Analysis processing package (Delene, 2011) was used  
to process the CAS, CDP, King hot-wire, and PCASP data. The University of Illinois/Oklahoma  
Optical Array Probe Processing Software (UIOOPS) (McFarquhar et al., 2018) was used to process



130 the 2D-S and HVPS-3 data. A merged droplet size distribution was calculated using the CAS or  
CDP dataset for  $3 < D < 50 \mu\text{m}$ , the 2D-S dataset for  $50 < D < 1050 \mu\text{m}$ , and the HVPS-3 dataset  
for  $D > 1050 \mu\text{m}$ .  $N_c$  was calculated by integrating droplet  $n(D)$  from the merged size distribution.  
Each 1 Hz data sample with  $N_c > 10 \text{ cm}^{-3}$  and King LWC  $> 0.05 \text{ g m}^{-3}$  was identified as in-cloud.  $N_a$   
was calculated by integrating the PCASP  $n(D)$  for out of cloud data samples.

135 Due to overlapping measurement ranges, the CAS, the CDPs, and the PDI provided at least  
two independent measurements of  $n(D)$  for  $3 < D < 50 \mu\text{m}$  during each flight (G22). Data from  
one probe was chosen for inclusion in the merged size distribution based on availability of valid  
measurements from the CAS, CDP or PDI and through comparisons between  $N_c$  and LWC from  
the CAS, CDP, and PDI datasets. The CAS was used to represent droplets with  $3 < D < 50 \mu\text{m}$  for  
140 research flights from ORACLES 2016 and the CDP for research flights from ORACLES 2017 and  
2018 (see G22 for justification and more details). The CAS  $n(D)$  for ORACLES 2016 was scaled  
using the King LWC for reference due to a potential sizing bias based on comparisons between  
the CAS LWC, CDP LWC, and King LWC (G22). The methodology for scaling the 2016 CAS  $n(D)$  is  
described in Appendix A along with its impact on this study. The uncertainties associated with  
145 the in situ measurements of  $N_c$ ,  $R_e$ , and  $\tau$  are discussed in Appendix B.

For each profile, cloud top height ( $Z_T$ ) and cloud base height ( $Z_B$ ) were defined as the  
highest and the lowest altitude, respectively, with  $N_c$  and King LWC greater than  $10 \text{ cm}^{-3}$  and  $0.05$   
 $\text{g m}^{-3}$ , respectively (G21). Cloud thickness ( $H$ ) was defined as the difference between  $Z_T$  and  $Z_B$ .  $R_e$   
and the effective variance ( $V_e$ ) for the merged size distribution were calculated following Hansen  
150 and Travis (1974) as



$$R_e(h) = \frac{1}{2} \int_3^{19200} D^3 n(D, h) dD / \int_0^{\infty} D^2 n(D, h) dD$$

and

$$V_e(h) = \int_3^{19200} (D - 2R_e(h))^2 D^2 n(D, h) dD / (2R_e(h))^2 \int_0^{\infty} D^2 n(D, h) dD \quad (1)$$

$R_e$  can also be defined in terms of  $R_v$  (mean volume radius) as

$$155 \quad R_e = k^{-1/3} R_v, \quad k = (1 + d^2)^3 / (ad^3 + 1 + 3d^2)^2, \quad (2)$$

where  $k$  is the droplet spectral width which is a function of the skewness ( $a$ ) and dispersion ( $d$ ) of the droplet size distribution (Martin et al., 1994).  $k$  can vary depending on aerosol conditions, occurrence of drizzle, cloud adiabaticity, and height in cloud (McFarquhar and Heymsfield, 2001; Brenguier et al., 2011). LWC was calculated as

$$160 \quad LWC(h) = \pi \rho_w / 6 \int_3^{19200} D^3 n(D, h) dD = 4/3 \pi \rho_w N_c(h) R_v(h)^3 \quad (3)$$

where  $h$  is height above  $Z_B$  and  $\rho_w$  is the liquid water density. At a height  $h$  in cloud, LWC is a function of the average  $N_c$  and  $R_v$  following Eq. (3). Liquid water path (LWP) and King LWP were calculated by integrating LWC and King LWC over  $h$  from  $Z_B$  to  $Z_T$ .  $\tau$  was calculated as

$$\beta_{ext}(h) = \int_3^{19200} Q_{ext} \pi/4 D^2 n(D, h) dD, \quad \tau = \int_{Z_B}^{Z_T} \beta_{ext}(h) dh, \quad (4)$$

165 where  $\beta_{ext}$  is the cloud extinction and the extinction efficiency ( $Q_{ext}$ ) for cloud droplets is assumed to be 2 (Hansen and Travis, 1974) in the limit of geometric optics. The integrals in Eq. (1), (3), and (4) were converted to discrete sums corresponding to the cloud probe size bins for  $D > 3 \mu\text{m}$  with a maximum drop size limit of 19200  $\mu\text{m}$ .





## 2.2 Satellite Retrievals

170 The MODIS instrument onboard Terra and Aqua acquires passive retrievals of radiance at  
non-absorbing and liquid water absorbing spectral bands (Platnick et al., 2003).  $R_e$  and  $\tau$  are  
retrieved using the bispectral retrieval method with the 0.86  $\mu\text{m}$  band paired with the 1.6, 2.1,  
or 3.7  $\mu\text{m}$  band (Nakajima and King, 1990).  $R_e$  and  $\tau$  from the MODIS Collection 6/6.1 Level 2  
product (C6) (Platnick et al., 2017a) at 1 km resolution are used. Three retrievals were made for  
175  $R_e$  ( $R_{e16}$ ,  $R_{e21}$ , and  $R_{e37}$ ) by pairing the 0.86  $\mu\text{m}$  band with the 1.6, 2.1, and 3.7  $\mu\text{m}$  band,  
respectively. Consistent with previous studies (e.g., PZ11),  $R_{e21}$  was used as the primary retrieval  
and MODIS  $R_e$  hereafter refers to  $R_{e21}$ . The wavelength dependence of MODIS  $\tau$  is not examined  
as  $\tau$  is mainly determined by the reflectance from the non-absorbing band (King et al., 1998).

$R_{e16}$ ,  $R_{e21}$ , and  $R_{e37}$  represent  $R_e$  at 2 to 4 optical depths below cloud top depending on  
180 liquid water absorption and a weighting function based on vertical penetration of photons into  
cloud (McFarquhar and Heymsfield, 1998; Platnick, 2000).  $R_{e37}$  corresponds to the level closest  
to cloud top followed by  $R_{e21}$  and  $R_{e16}$  in order of increasing distance from cloud top. In an  
upgrade from the MODIS Collection 5.1 (C5) product, which reported  $R_{e21}$ ,  $R_{e21}$  minus  $R_{e16}$ , and  
 $R_{e21}$  minus  $R_{e37}$ , the MODIS C6 product reported  $R_{e16}$ ,  $R_{e21}$ , and  $R_{e37}$  separately. Thus, biases in  $R_{e16}$   
185 and  $R_{e37}$  associated with the condition of a successful  $R_{e21}$  retrieval are removed (Platnick et al.,  
2017b) and  $R_{e16}$ ,  $R_{e21}$ , and  $R_{e37}$  can be compared (Section 3). Within the ORACLES sampling  
domain (10° W to 15° E and 5° N to 20° S; Fig. 1),  $R_{e16}$ ,  $R_{e21}$ , and  $R_{e37}$  from the C6 product can be  
up to 2  $\mu\text{m}$  lower than the corresponding retrievals from the C5 product (Rausch et al., 2017).



The MODIS retrievals are integrated quantities which do not describe the vertical  
190 structure of the cloud. In the absence of in situ data, the vertical profile of LWC and  $R_v$  can be  
approximated using the adiabatic model to parameterize  $N_c$  and LWP as a function of  $\tau$  and  $R_e$   
(Brenguier et al., 2000; Szczodrak et al., 2001). The adiabatic LWC was defined as

$$LWC_{ad}(h) = C_w h = 4/3 \pi \rho_w N_{ad}(h) R_{vad}(h)^3, \quad (5)$$

where  $C_w$  is the condensation rate, and the subscript 'ad' represents the adiabatic equivalent of  
195 a variable. Equations (1) to (4) were combined with Eq. (5) to determine  $\tau_{ad}$  and  $LWP_{ad}$  following  
Brenguier et al. (2000) and Szczodrak et al. (2001), respectively, as

$$\tau_{ad} = 3/5 \pi Q_{ext} (3 C_w / 4 \pi \rho_w)^{2/3} (k N_c)^{1/3} H^{5/3} \text{ and}$$
$$LWP_{ad} = 1/2 C_w H^2 = 5/9 \rho_w \tau R_e. \quad (6)$$

Using Equation (5),  $N_c$  was parameterized in terms of  $\tau$  and  $R_e$  following Szczodrak et al.  
200 (2001) as

$$N_c = \sqrt{10}/4 \pi k (\alpha C_w \tau / \rho_w R_e^5)^{1/2}, \quad (7)$$

where  $\alpha$  is the adiabaticity defined as LWP divided by  $LWP_{ad}$ . MODIS  $N_c$  was calculated using  
MODIS  $R_e$  and  $\tau$  based on Eq. (7).

### 2.3 Data Selection and Co-location

205 MODIS data with valid retrievals within the ORACLES sampling domain (10° W to 15° E  
and 5° N to 20° S; Fig. 1) were used. The Terra and Aqua satellites overpass the Equator at about  
10:30 and 13:30 local time, respectively. Most cloud profiles from ORACLES were flown within 1



to 2 hours of 12:00 UTC. The time gap between the MODIS scan and the in situ sampling for a cloud profile was designated as  $\Delta T$ . The analysis was limited to cloud profiles with a co-located  
210 MODIS retrieval with  $\Delta T$  less than 3600 s. This assumes that the cloud layer did not undergo significant changes within one hour. This assumption was tested by comparing MODIS retrievals against in situ measurements for different upper bounds of  $\Delta T$  (Section 3).

MODIS retrievals were co-located with in situ data following the criteria outlined by PZ11. The pixel closest to the cloud top latitude and longitude during a cloud profile was selected. The  
215 location of the selected pixel was adjusted to account for advection of the cloud field using the mean wind speed and direction during the profile from the Turbulent Air Motion Measurement System (Thornhill et al., 2003) on the NASA P-3 aircraft. The wind speed was between 5 to 10 m  $s^{-1}$ , which meant the pixel location was adjusted by a distance of up to 18 to 36 km over an hour, on average. The MODIS  $R_e$  and  $\tau$  were averaged over a 5 x 5 pixel domain centered on the  
220 adjusted pixel to account for spatial inhomogeneity. The profile was rejected if the pixel after adjusting for advection was less than 3 pixels from the edge of the MODIS scan and if more than 10 % of the retrievals within the 5 x 5 pixel domain, i.e., at least three out of the 25 pixels, were invalid. Estimates of  $Z_T$  and cloud top temperature ( $T_T$ ) from the MODIS C6 product were used to limit the analysis to warm, boundary layer clouds. Four profiles were excluded from the analysis  
225 since the MODIS  $Z_T$  was greater than 2500 m or MODIS  $T_T$  was less than 273 K.

With the above criteria, at least one cloud profile from 21 research flights conducted during ORACLES had a co-located MODIS retrieval with  $\Delta T < 3600$  s (Table 1). There were 74 cloud profiles with co-located MODIS Terra retrievals and 71 cloud profiles with co-located MODIS



Aqua retrievals (Table 2).  $\Delta T$  was evenly distributed with 10 to 15 cloud profiles within every 300  
230 s bin from 0 to 3600 s (except 1200 to 1800 s) (Fig. 2a). For 97 out of the 145 cloud profiles, the  
distance between the cloud profile location and the MODIS pixel after adjusting for advection  
was below 12 km (Fig. 2b). The distance was greater than 36 km for five profiles.

### 3 MODIS versus In situ

#### 3.1 $R_e$ Comparisons

235 MODIS  $R_e$  was compared with the in situ  $R_e$  averaged over the top 10 % of the cloud layer  
sampled during cloud profiles with a co-located MODIS retrieval with  $\Delta T < 3600$  s (Fig. 3a). The  
difference between MODIS  $R_e$  and in situ  $R_e$  for a cloud profile was termed  $\Delta R_e$  with positive  $\Delta R_e$   
indicating that MODIS  $R_e$  was greater than in situ  $R_e$ . The average MODIS  $R_e$  (11.3  $\mu\text{m}$ ) was greater  
than the average in situ  $R_e$  (9.7  $\mu\text{m}$ ) with Pearson's correlation coefficient ( $R$ ) = 0.77 and root  
240 mean square error (RMSE) = 2.5  $\mu\text{m}$ . All but 12 cloud profiles had positive  $\Delta R_e$ . The average  $\Delta R_e$   
was  $1.6 \pm 1.8$   $\mu\text{m}$  where the uncertainty estimate represents the sum of the average retrieval  
uncertainty for MODIS  $R_e$  from the C6 product and the measurement uncertainty for the average  
in situ  $R_e$  (Appendix B). Previous comparisons between airborne measurements and MODIS  
retrievals of  $R_e$  for warm clouds have shown similar  $\Delta R_e$  values. For example, the MODIS  $R_e$  and  
245 in situ  $R_e$  with  $\Delta T < 3600$  s for marine stratocumulus over the southeast Pacific had an average  
 $\Delta R_e$  of 2.1  $\mu\text{m}$  (PZ11). The MODIS  $R_e$  and in situ  $R_e$  with  $\Delta T < 1500$  s for liquid clouds over the  
North Atlantic had an average  $\Delta R_e$  of 1.7  $\mu\text{m}$  (Painemal et al., 2021).

There were 104 profiles with  $\Delta R_e$  less than  $\pm 2$   $\mu\text{m}$  while eight profiles had  $\Delta R_e > 5$   $\mu\text{m}$   
(Fig. 4a).  $\Delta R_e$  was well correlated with MODIS  $R_e$  ( $R = 0.62$ ) and seven out of eight profiles with



250  $\Delta R_e > 5 \mu\text{m}$  had MODIS  $R_e > 15 \mu\text{m}$  (Fig. 4a). The average  $\Delta R_e$  and RMSE decreased from 1.6 to 1.4 and 2.5 to 1.8, respectively, when 13 profiles with MODIS  $R_e > 15 \mu\text{m}$  were removed. The MODIS  $R_e$  retrieval uncertainty (5 % to 15 %) was poorly correlated with  $\Delta R_e$  (Fig. 4b). For lower bounds of  $\Delta T$ , the average  $\Delta R_e$  and RMSE decreased and the correlation between MODIS  $R_e$  and in situ  $R_e$  increased (Table 3). The 42 cloud profiles with a co-located MODIS retrieval with  $\Delta T <$   
255 900 s had three profiles with  $\Delta R_e > 5 \mu\text{m}$  (Fig. 3b). All three of these profiles were associated with MODIS  $R_e > 15 \mu\text{m}$ .

MODIS  $R_e$  for five out of the eight profiles with  $\Delta R_e > 5 \mu\text{m}$  was retrieved by MODIS Aqua. Consequently, retrievals from MODIS Aqua had higher average  $\Delta R_e$  and lower correlation with in situ  $R_e$  compared to retrievals from MODIS Terra (Table 3). This was despite the lower average  
260  $\Delta T$  for retrievals from MODIS Aqua (1650 s) compared to retrievals from MODIS Terra (2020 s). The solar ( $\mu_0$ ) and sensor ( $\mu$ ) zenith angles for MODIS Aqua and MODIS Terra were obtained from the MODIS C6 product. There were minor differences between the average  $\mu_0$  and  $\mu$  for MODIS Terra (24.0° and 43.0°) and MODIS Aqua (29.7° and 40.0°) (Fig. 5). The MODIS  $R_e$  and  $\Delta R_e$  had weak correlations with  $\mu_0$  ( $R = 0.18$  and  $0.16$ ) and  $\mu$  ( $R = -0.05$  and  $-0.09$ ) which suggests  $\mu_0$  and  
265  $\mu$  had little impact on the performance of MODIS Terra relative to MODIS Aqua.

$R_{e16}$ ,  $R_{e21}$ , and  $R_{e37}$  were compared (Fig. 6) to determine whether  $\Delta R_e$  was dependent on the use of  $R_{e21}$  as the primary retrieval. The average  $R_{e16}$ ,  $R_{e21}$ , and  $R_{e37}$  were 10.4, 11.3, and 11.7  $\mu\text{m}$ , respectively. The average  $R_{e16}$  and  $R_{e21}$  had statistically significant differences while the average  $R_{e21}$  and  $R_{e37}$  had statistically insignificant differences. The latter was consistent with  
270 global analyses that found  $R_{e37}$  minus  $R_{e21}$  depends on cloud regime with positive values (0 to 0.6



$\mu\text{m}$ ) for homogeneous marine stratocumulus (Zhang and Platnick, 2011; Fu et al., 2019). Differences between  $R_{e16}$ ,  $R_{e21}$ , and  $R_{e37}$  are associated with differences in the vertical penetration of photons into the cloud. The penetration depth decreases with increasing wavelength from 1.6 to 3.7  $\mu\text{m}$  (Platnick, 2000). An increase in  $R_e$  with height in cloud (G22) resulted in  $R_{e16} < R_{e21} <$   
275  $R_{e37}$ . Although  $R_{e21}$  minus  $R_{e37}$  depends on  $\mu_0$ , the average  $\mu_0$  for ORACLES (26.8°) was lower than the range of  $\mu_0$  (65 to 70°) for which  $R_{e37}$  minus  $R_{e21}$  exceeds 1  $\mu\text{m}$  (Grosvenor and Wood, 2014). Consistent with Zhang and Platnick (2011), the correlation between  $R_{e21}$  and  $R_{e16}$  (or  $R_{e37}$ ) decreased for values above 15  $\mu\text{m}$  (Fig. 6). For values below 15  $\mu\text{m}$ ,  $R_{e16}$ ,  $R_{e21}$ , and  $R_{e37}$  had an average of 9.9, 10.8, and 11.1  $\mu\text{m}$ , respectively, and high correlation between  $R_{e16}$  and  $R_{e21}$  ( $R =$   
280 0.92) and  $R_{e21}$  and  $R_{e37}$  ( $R = 0.95$ ). Thus, MODIS  $R_e$  had a positive bias regardless of the retrieval wavelength. On average,  $R_{e21}$  had lower retrieval uncertainty (0.8  $\mu\text{m}$ ) compared to  $R_{e16}$  (1.9  $\mu\text{m}$ ) and  $R_{e37}$  (1.1  $\mu\text{m}$ ) which suggests  $R_{e21}$  gives a robust estimate of the average  $\Delta R_e$ .

Since each MODIS  $R_e$  retrieval penetrates a certain optical depth into cloud, the altitude and in situ  $R_e$  at the level of 2 optical depths below cloud top ( $Z_{\tau 2}$  and  $R_{e\tau 2}$ ) were compared with  
285 the altitude and in situ  $R_e$  averaged over the top 10 % of the cloud ( $R_{e10}$  and  $Z_{10}$ ).  $R_{e\tau 2}$  and  $R_{e10}$  were strongly correlated ( $R = 0.87$ ) with average values of 9.4 and 9.7  $\mu\text{m}$ , respectively (Fig. 7a).  $R_{e\tau 2}$  was less than  $R_{e10}$  because the average  $Z_{\tau 2}$  was 17 m lower than  $Z_{10}$  (Fig. 7b) and  $R_e$  increased with height in cloud (G22). When five profiles with  $R_e > 15 \mu\text{m}$  were removed,  $R_{e\tau 2}$  and  $R_{e10}$  had average values of 9.3 and 9.4  $\mu\text{m}$ , respectively, with improved correlation ( $R = 0.95$ ). The average  
290 difference between  $R_{e\tau 2}$  and  $R_{e10}$  (0.3  $\mu\text{m}$ ) was lower than the average  $\Delta R_e$  between MODIS  $R_e$  and  $R_{e10}$  (1.7  $\mu\text{m}$ ). Thus, the choice of  $R_{e10}$  did not have a large impact on the average  $\Delta R_e$ .



### 3.2 $\tau$ Comparisons

For profiles with a co-located MODIS retrieval with  $\Delta T < 3600$  s, the average MODIS  $\tau$  (11.7) was greater than the average in situ  $\tau$  (9.4) with  $R = 0.73$  and RMSE = 5.2 (Fig. 8a).  $\Delta\tau$  was defined as the difference between MODIS  $\tau$  and in situ  $\tau$  for a cloud profile with positive values indicating that MODIS  $\tau$  was higher. The average  $\Delta\tau$  was  $2.3 \pm 3.4$  where the uncertainty estimate represents the sum of the average retrieval uncertainty for MODIS  $\tau$  from the C6 product and the measurement uncertainty for the average in situ  $\tau$  (Appendix B). Nine profiles with MODIS  $\tau > 25$  had an average  $\Delta\tau$  of 8.1 with six of the profiles having  $\Delta\tau > \pm 10$ . When profiles with MODIS  $\tau > 25$  were removed, the average  $\Delta\tau$  and RMSE decreased from 2.3 to 2.0 and 5.2 to 4.2, respectively. Retrievals from MODIS Terra had lower  $\Delta\tau$  and better correlation with in situ  $\tau$  compared to retrievals from MODIS Aqua (Table 3). The average  $\Delta\tau$  decreased and the correlation between MODIS  $\tau$  and in situ  $\tau$  improved for profiles with lower  $\Delta T$  (Table 3). This is consistent with time-dependent improvement in correlations between MODIS  $\tau$  and  $\tau$  retrieved using the airborne Solar Spectral Flux Radiometer during ORACLES (Chang et al., 2021).

Profiles with a co-located MODIS retrieval with  $\Delta T < 900$  s had  $\Delta\tau = 1.4$ ,  $\sigma(\tau) = 2.2$ , and MODIS  $\tau$  uncertainty = 0.6, on average. For 24 out of the 42 profiles with a co-located MODIS retrieval with  $\Delta T < 900$  s,  $\Delta\tau$  was greater than  $\pm 2$  (Fig. 8b). A single profile with  $\Delta T < 900$  s had MODIS  $\tau > 25$  which was associated with  $\Delta\tau$  of -14.6. MODIS  $\tau$  can have biases relative to in situ  $\tau$  due to spatial heterogeneity of the cloud field or MODIS  $\tau$  retrieval uncertainties. On average, MODIS  $\tau$  had a standard deviation ( $\sigma(\tau)$ ) of 2.2 over the 25 pixel domain for each cloud profile and  $\sigma(\tau)$  was correlated with MODIS  $\tau$  ( $R = 0.72$ ). The  $\Delta\tau$  increased with MODIS  $\tau$  (Fig. 9a) and the



MODIS  $\tau$  retrieval uncertainty increased with MODIS  $\tau$  (Fig. 9b). The latter is expected given a decrease in the sensitivity of  $\tau$  to the non-absorbing reflectance as  $\tau$  increases (King et al., 1998).  
315 However, the average retrieval uncertainty for MODIS  $\tau$  (0.6) was less than the average  $\Delta\tau$  (2.3).

### 3.3 $N_c$ Comparisons

$N_c$  calculated using MODIS  $R_e$  and  $\tau$  in Eq. (7) (hereafter, MODIS  $N_c$ ) was compared with in situ  $N_c$ . Figure 10 shows cloud properties as a function of normalized height above cloud base ( $Z_N$ ) where  $Z_N$  equals  $Z - Z_B$  divided by  $Z_T - Z_B$ . The in situ  $N_c$  was averaged over the top half of the  
320 cloud layer since entrainment mixing led to lower  $N_c$  over the top 10 % of the cloud height (Fig. 10a). Cloud-top entrainment did not affect  $R_e$  near cloud top (Fig. 10b) and hence did not impact the comparisons between MODIS and in situ  $R_e$ . Eight profiles with MODIS  $\tau < 5$  were removed from the  $N_c$  comparisons to avoid the impact of higher variability in MODIS retrievals for optically thin clouds (Zhang and Platnick, 2011). The exclusion of these profiles did not lead to significant  
325 changes in the  $R_e$  or  $\tau$  comparisons.

$\Delta N_c$  was defined as the difference between MODIS  $N_c$  and in situ  $N_c$  for a cloud profile with positive  $\Delta N_c$  indicating that MODIS  $N_c$  was higher. For 137 profiles with a co-located MODIS retrieval with  $\Delta T < 3600$  s and MODIS  $\tau > 5$ , the average MODIS  $N_c$  ( $151 \text{ cm}^{-3}$ ) had good agreement with the average in situ  $N_c$  ( $151 \text{ cm}^{-3}$ ) with  $R = 0.90$  and  $\text{RMSE} = 38 \text{ cm}^{-3}$  (Fig. 11). The average  $\Delta N_c$   
330 was  $0 \pm 64 \text{ cm}^{-3}$  where the uncertainty estimate represents the sum of the error in calculating the average MODIS  $N_c$  (Section 3.3.3) and the measurement uncertainty for the average in situ  $N_c$  (Appendix B). In comparison, stratocumulus over the southeast Pacific had an average  $\Delta N_c$  of  $-4 \text{ cm}^{-3}$  with  $R = 0.94$  (PZ11).





Unlike the  $R_e$  or  $\tau$  comparisons, lower  $\Delta T$  was not associated with lower  $\Delta N_c$  or better  
335 correlation between MODIS and in situ  $N_c$ . Further, MODIS Aqua  $N_c$  and MODIS Terra  $N_c$  had  
similar performance relative to in situ  $N_c$  (Table 3). There were 15 profiles with  $\Delta N_c$  greater than  
 $\pm 50 \text{ cm}^{-3}$  (average  $\Delta N_c = 2 \text{ cm}^{-3}$  and RMSE =  $89 \text{ cm}^{-3}$ ). These profiles were associated with higher  
variability in the in situ data with an average standard deviation of  $68 \text{ cm}^{-3}$  for the in situ  $N_c$ .  
Similarly, the three profiles with  $\Delta N_c > \pm 100 \text{ cm}^{-3}$  had an average standard deviation of  $86 \text{ cm}^{-3}$   
340 for the in situ  $N_c$ . The correlation between MODIS  $N_c$  and in situ  $N_c$  increased to 0.93 and the  
RMSE decreased to  $31 \text{ cm}^{-3}$  when these three profiles were removed. For 50 % of the profiles,  
 $\Delta N_c$  was below  $\pm 20 \text{ cm}^{-3}$  which highlights the validity of the adiabatic assumption (Brenguier et  
al., 2000; Szczodrak et al., 2001) and the precision of the in situ estimates of  $k$ ,  $C_w$ , and  $\alpha$  (0.76,  
 $2.94 \text{ g m}^{-3} \text{ km}^{-1}$ , and 0.74). The agreement between the average MODIS  $N_c$  and in situ  $N_c$  was  
345 driven by compensating uncertainties associated with the parameters used in Eq. (7). These  
uncertainties were examined along with their impact on the calculation of MODIS  $N_c$ .

### 3.3.1 Uncertainties associated with, $C_w$ , $\alpha$ , and $k$

MODIS does not retrieve the vertical profile of LWC. Parameters that represent the  
estimated rate of condensation with height in cloud ( $C_w$ ) and the ratio of the vertical integrals of  
350 LWC and  $\text{LWC}_{\text{ad}}$  ( $\alpha$ ) can provide the largest sources of error in MODIS  $N_c$  (Janssen et al., 2011;  
Min et al., 2012).  $\alpha$  had a negative correlation with  $H$  (Fig. 12) (Min et al., 2012; Braun et al., 2018)  
and  $C_w$  was a function of cloud base pressure and temperature (Brenguier et al., 2000). Based on  
the range of estimates in the existing literature,  $C_w$  and  $\alpha$  contribute a factor ranging from 0.9 to  
1.5 in Eq. (7) (Merk et al., 2016, and references therein). For 142 profiles with a co-located MODIS



355 retrieval with  $\Delta T < 3600$  s and  $LWP_{ad} > 5$  g m<sup>-2</sup>, the average  $C_w$  and  $\alpha$  were  $2.94 \pm 0.21$  g m<sup>-3</sup> km<sup>-1</sup>  
and  $0.74 \pm 0.26$ , respectively, where the uncertainty estimates represent one standard deviation.  
These values of  $C_w$  and  $\alpha$  resulted in a factor of 1.47 in Eq. (7). In comparison, PZ11 assumed  $C_w$   
= 2 g m<sup>-3</sup> km<sup>-1</sup> and  $\alpha = 1$  with  $C_w$  and  $\alpha$  contributing a factor of 1.41 in Eq. (7). Using  $C_w = 2$  and  $\alpha$   
= 1 in Eq. (7) would decrease MODIS  $N_c$  and the average  $\Delta N_c$  would change to - 6 cm<sup>-3</sup> (from 0.1  
360 cm<sup>-3</sup> when  $C_w = 2.94$  and  $\alpha = 0.74$  were used) while the RMSE remained unchanged.

$k$  represents spectral width which decreases when droplet size distributions get narrower.  
Consistent with PZ11,  $k$  averaged over the top 10 % of the cloud layer ( $0.76 \pm 0.12$ ) was higher  
than  $k$  averaged over the entire cloud layer ( $0.70 \pm 0.15$ ) (Fig. 13), where the uncertainty  
estimates represent one standard deviation. Since MODIS  $R_e$  corresponds to values near cloud  
365 top,  $k = 0.76$  was used in Eq. (7). Using  $k = 0.70$  would increase MODIS  $N_c$  and the average  $\Delta N_c$   
and RMSE would change to 13 cm<sup>-3</sup> and 42 cm<sup>-3</sup>, respectively (from 0 cm<sup>-3</sup> and 38 cm<sup>-3</sup> when  $k =$   
0.76 was used). The value of cloud top  $k$  (0.76) was consistent with the  $k$  calculated for marine  
clouds with entrainment mixing where  $k$  decreased when  $\alpha$  decreased (Brenguier et al., 2011).  
In comparison, higher  $k$  (0.8) has been calculated for marine clouds without entrainment mixing  
370 (Martin et al., 1994). The decrease in  $N_c$  and LWC near cloud top with increasing  $R_e$  was indicative  
of inhomogeneous mixing (Fig. 10) and spectral broadening due to entrainment or drizzle (Sinclair  
et al., 2021) would explain the higher values for  $k$  near cloud top (Fig. 13).

### 3.3.2 Uncertainties associated with MODIS $R_e$ and $\tau$

The MODIS algorithm assumes vertically homogeneous  $R_e$  and LWC (King et al., 1998) but  
375  $R_e$  and LWC increased almost linearly with height (LWC decreased near cloud top due to



entrainment mixing) (Fig. 10b, c). The impact of this inconsistency was examined by quantifying  $\Delta N_c$  for profiles with large MODIS biases in  $R_e$  or  $\tau$ . The average  $\Delta N_c$  for nine profiles with MODIS  $\tau > 25$  (average  $\Delta \tau = 8.1$ ) and 10 profiles with MODIS  $\tau > 5$  and MODIS  $R_e > 15 \mu\text{m}$  (average  $\Delta R_e = 4.4 \mu\text{m}$ ) was  $-8$  and  $-15 \text{ cm}^{-3}$ , respectively. The magnitude of  $\Delta N_c$  was greater than  $50 \text{ cm}^{-3}$  for only two profiles with MODIS  $\tau > 25$  and zero profiles with MODIS  $R_e > 15 \mu\text{m}$ . This suggests a large bias in MODIS  $R_e$  or  $\tau$  did not necessarily result in a large bias in MODIS  $N_c$ .

The MODIS algorithm used a modified gamma distribution function to represent the droplet spectrum assuming  $V_e$  (Eq. 1) to be 10 % (Platnick et al., 2017b). For such size distributions,  $k$  is related to  $V_e$  as  $k = (1-V_e) \times (1-2V_e)$  and  $V_e = 10 \%$  corresponds to  $k = 0.72$  (Grosvenor et al., 2018). For ORACLES,  $V_e$  decreased with height (Fig. 10d) with a median cloud top  $V_e$  of 8.4 % corresponding to  $k = 0.76$ . The a priori assumption of  $V_e = 10 \%$  could lead to biases of up to  $1 \mu\text{m}$  for MODIS  $R_e$  (Chang and Li, 2002). Radiative transfer simulations to quantify the MODIS  $R_e$  bias associated with  $V_e$  were beyond the scope of this study. It is assumed the uncertainties associated with instrument error and atmospheric corrections were included in the retrieval uncertainty estimates in the MODIS C6 product.

The presence of drizzle could introduce biases in MODIS  $R_e$  or  $N_c$  due to lower  $k$  associated with spectral broadening (Sinclair et al., 2021), higher  $V_e$  for a bimodal size distribution (Nakajima et al., 2010), or lower  $\alpha$  due to cloud water removal through precipitation (Braun et al., 2018). However, the average rain rate for ORACLES was too low ( $0.06 \text{ mm h}^{-1}$ ) (G22) for drizzle to have a major impact on the  $R_e$  retrievals (Zinner et al., 2010; PZ11). This was supported by the positive values for  $R_{e37}$  minus  $R_{e21}$  which represent size distributions without a significant drizzle mode



(Nakajima et al., 2010). The impact of cloud water removal through precipitation was included by using the in situ  $\alpha$  (0.74) in Eq. (7).

### 3.3.3 MODIS $N_c$ Error Analysis

400 The total error for MODIS  $N_c$  from Eq. (7) was quantified using the propagation of measurement uncertainties associated with  $k$ ,  $C_w$ , and  $\alpha$ , and retrieval uncertainties associated with MODIS  $R_e$  and  $\tau$ . Assuming the covariances were normally distributed and random, the total error can be calculated using Gaussian error propagation as

$$\left(\frac{\delta N_c}{N_c}\right)^2 = \left(\frac{1}{2} \frac{\delta \tau}{\tau}\right)^2 + \left(\frac{5}{2} \frac{\delta R_e}{R_e}\right)^2 + \left(\frac{1}{2} \frac{\delta C_w}{C_w}\right)^2 + \left(\frac{1}{2} \frac{\delta \alpha}{\alpha}\right)^2 + \left(\frac{\delta k}{k}\right)^2, \quad (8)$$

405 where  $\delta$  represents the error for each variable. For MODIS  $R_e$  and  $\tau$ , the error was defined as the average retrieval uncertainty from the MODIS C6 product (7.5 and 5 %, respectively). For  $k$ ,  $C_w$ , and  $\alpha$ , the error was defined as one standard deviation (16, 7.1, and 35 % of their averages).

Based on Eq. (8), MODIS  $N_c$  had an error of 30.5 %. This was smaller than previous estimates of 38 % (Janssen et al., 2011) and 78 % (Grosvenor et al., 2018). Consistent with  
410 Grosvenor et al. (2018),  $R_e$  was the parameter with the largest contribution to the total error in MODIS  $N_c$  followed by  $\alpha$  and  $k$ . Profiles with MODIS  $R_e > 15 \mu\text{m}$  and average  $\Delta R_e$  of  $4.4 \mu\text{m}$  had an average  $\Delta N_c$  of  $-15 \text{ cm}^{-3}$  highlighting the compensation of the  $R_e$  uncertainty Eq. (7) by the other parameters. MODIS  $N_c$  calculated using in situ estimates of  $k$ ,  $C_w$ , and  $\alpha$  from ORACLES was higher than the MODIS  $N_c$  determined using a priori assumptions for  $k$ ,  $C_w$ , and  $\alpha$ . For example,  
415 substituting  $C_w = 2 \text{ g m}^{-3} \text{ km}^{-1}$  and  $\alpha = 1$  (PZ11) and  $k = 0.8$  (Martin et al., 1994) in Eq. (7) would introduce a factor which was 9 % lower than using  $C_w = 2.94 \text{ g m}^{-3} \text{ km}^{-1}$ ,  $\alpha = 0.74$ , and  $k = 0.76$ .



The MODIS  $N_c$  calculated based on these a priori assumptions would have average  $\Delta N_c$  and RMSE of  $-14 \text{ cm}^{-3}$  and  $39 \text{ cm}^{-3}$ , respectively (compared to  $0 \text{ cm}^{-3}$  and  $38 \text{ cm}^{-3}$  using the in situ estimates).

#### 4 Aerosol-cloud Interactions

420 During the ORACLES research flights, variable vertical separation was observed between biomass burning aerosols from southern Africa and marine stratocumulus over the southeast Atlantic (Redemann et al., 2021). Cloud profiles were conducted at locations of both contact and separation between the base of the aerosol layer and the top of the cloud layer. Cloud profiles with aerosol concentration ( $N_a$ ) greater than  $500 \text{ cm}^{-3}$  within 100 m above cloud tops were 425 termed “contact profiles” and cloud profiles with  $N_a < 500 \text{ cm}^{-3}$  up to 100 m above cloud tops were termed “separated profiles” (G21).

Across the ORACLES campaigns, 173 contact profiles were conducted with  $84$  to  $90 \text{ cm}^{-3}$  higher in situ  $N_c$ ,  $1.4$  to  $1.6 \mu\text{m}$  lower in situ  $R_e$ , and  $0.04$  to  $3.06$  higher in situ  $\tau$  compared to 156 separated profiles (G22). These differences between in situ  $N_c$ ,  $R_e$ , and  $\tau$  for contact and 430 separated profiles were statistically significant ( $p < 0.02$ ) and their ranges represent the 95 % confidence intervals from a two-sample t-test. These confidence intervals represent the difference between the average values for contact and separated profiles determined with 95 % confidence. Given the statistically similar sea surface temperature, lower tropospheric stability, and estimated inversion strength at the locations of contact and separated profiles, the cloud 435 microphysical differences were attributed to aerosol-cloud interactions (G22).

A co-located MODIS retrieval with  $\Delta T$  less than 3600 s was available for 67 contact and 78 separated profiles (Table 1). These contact profiles had  $84$  to  $91 \text{ cm}^{-3}$  higher in situ  $N_c$ ,  $1.4$  to  $1.6$



$\mu\text{m}$  lower in situ  $R_e$ , and 0.44 to 4.64 higher in situ  $\tau$  compared to the separated profiles. When the in situ  $N_c$  and  $R_e$  were averaged over the top 50 % and top 10 % of the cloud, respectively, contact profiles had 87 to 98  $\text{cm}^{-3}$  higher in situ  $N_c$  and 1.5 to 2.1  $\mu\text{m}$  lower in situ  $R_e$  compared to separated profiles. Differences between the in situ  $N_c$ ,  $R_e$ , and  $\tau$  for contact and separated profiles were compared with corresponding differences between MODIS  $N_c$ ,  $R_e$ , and  $\tau$ . For simplicity, it is assumed the MODIS and in situ uncertainties were consistent for contact and separated profiles. This assumption allows direct comparison of MODIS estimates of the differences between cloud properties for contact and separated profiles with in situ estimates.

For contact profiles, the average MODIS  $R_e$  (9.9  $\mu\text{m}$ ) was 1.4  $\mu\text{m}$  greater than the average in situ  $R_e$  with  $R = 0.76$  (Fig. 14). In comparison, for separated profiles, the average MODIS  $R_e$  (12.6  $\mu\text{m}$ ) was 1.9  $\mu\text{m}$  larger than the average in situ  $R_e$  with  $R = 0.72$ . Separated profiles had a greater  $\Delta R_e$  compared to contact profiles because 12 out of 13 profiles with MODIS  $R_e > 15 \mu\text{m}$ , with high average  $\Delta R_e$  (4.0  $\mu\text{m}$ ) (Fig. 4a), were classified as separated profiles. As a result, the MODIS  $R_e$  estimate (2.6  $\mu\text{m}$ ) for the aerosol-induced increase in  $R_e$  from contact to separated profiles was greater than the in situ  $R_e$  estimate (2.1  $\mu\text{m}$ ). MODIS  $R_e$  had a similar positive bias for contact and separated profiles with MODIS  $R_e < 15 \mu\text{m}$  (1.3 and 1.5  $\mu\text{m}$ , respectively). Thus, when profiles with MODIS  $R_e > 15 \mu\text{m}$  were removed, the estimate of the  $R_e$  difference between contact and separated profiles using MODIS  $R_e$  and in situ  $R_e$  were closer (1.8  $\mu\text{m}$  and 1.6  $\mu\text{m}$ , respectively). Fewer profiles with  $R_e$  from MODIS Terra had MODIS  $R_e > 15 \mu\text{m}$  compared to MODIS Aqua and closer agreement was observed between the in situ  $R_e$  and MODIS  $R_e$  estimates of the aerosol-induced change in  $R_e$  for MODIS Terra compared to MODIS Aqua (Table 4).



For contact profiles, the average MODIS  $\tau$  (13.3) was 2.5 optical depths greater than the  
460 average in situ  $\tau$  with  $R = 0.75$  (Fig. 15). In comparison, for separated profiles, the average MODIS  
 $\tau$  (10.3) was 2.1 optical depths greater than the average in situ  $\tau$  with  $R = 0.62$ . As a result, the  
MODIS  $\tau$  estimate (3.0) was greater than the in situ  $\tau$  estimate (2.6) of the aerosol-induced  
increase in  $\tau$  from separated to contact profiles. Contact profiles with co-located MODIS Aqua  
retrievals had lower in situ  $\tau$  compared to separated profiles. The  $\tau$  from MODIS Aqua reproduced  
465 the sign and magnitude of this change (Table 4). The MODIS Terra  $\tau$  underestimated the in situ  
 $\tau$  increase from separated to contact profiles (Table 4) due to the profile with MODIS  $\tau > 25$  and  
 $\Delta\tau = -14.6$  (Fig. 15). All nine profiles with MODIS  $\tau > 25$  were classified as contact profiles (Fig.  
15). When these profiles were removed given their large average  $\Delta\tau$  (8.1), the remaining 58  
contact profiles had MODIS  $\tau$  (10.8) which was 1.6 optical depths greater than in situ  $\tau$  ( $R = 0.74$ ),  
470 on average. Subsequently, the MODIS  $\tau$  estimate (0.5) was less than the in situ  $\tau$  estimate (1.0)  
of the aerosol-induced increase in  $\tau$  from separated to contact profiles.

The average MODIS  $N_c$  for contact profiles ( $203 \text{ cm}^{-3}$ ) was  $2 \text{ cm}^{-3}$  lower than the average  
in situ  $N_c$  ( $R = 0.86$ ) (Fig. 16). For separated profiles, the average MODIS  $N_c$  ( $105 \text{ cm}^{-3}$ ) was  $2 \text{ cm}^{-3}$   
greater than the average in situ  $N_c$  ( $R = 0.82$ ). This meant the estimate for the aerosol-induced  
475 increase in  $N_c$  (from separated to contact profiles) from MODIS  $N_c$  ( $99 \text{ cm}^{-3}$ ) was similar to the  
estimate from in situ  $N_c$  ( $103 \text{ cm}^{-3}$ ). The three profiles with  $\Delta N_c > \pm 100 \text{ cm}^{-3}$  were classified as  
contact profiles. When these profiles were removed, estimates for the aerosol-induced increase  
in  $N_c$  from separated to contact profiles from MODIS  $N_c$  and in situ  $N_c$  were similar ( $95 \text{ cm}^{-3}$  and  
 $94 \text{ cm}^{-3}$ , respectively). For MODIS Terra retrievals, underestimation of the increase in in situ  $N_c$



480 from separated to contact profiles (Table 4) was driven by the profile with  $\Delta\tau = -14.6$  and MODIS  
 $\tau > 25$  (Fig. 15). When this profile was removed, the MODIS  $N_c$  and in situ  $N_c$  estimates were  
within  $5 \text{ cm}^{-3}$ . The MODIS  $N_c$  calculated using a priori assumptions for  $k$ ,  $C_w$ , and  $\alpha$  underestimated  
the in situ  $N_c$  for contact profiles (by  $20 \text{ cm}^{-3}$ ) and separated profiles (by  $8 \text{ cm}^{-3}$ ). The a priori  
MODIS  $N_c$  estimate ( $91 \text{ cm}^{-3}$ ) for the increase in  $N_c$  from separated to contact profiles was slightly  
485 lower than the in situ  $N_c$  estimate ( $103 \text{ cm}^{-3}$ ).

## 5 Discussion

Differences between climate model and observational estimates of the effective radiative  
forcing due to ACI are largely driven by uncertainties in observational estimates of the radiative  
forcing due to aerosol effects on cloud albedo ( $\text{RF}_{\text{aci}}$ ) (Gryspeerd et al., 2020). Issues with satellite  
490 estimates of  $\text{RF}_{\text{aci}}$  persist due to biases in satellite retrievals of  $N_c$  (Grosvenor et al., 2018), above-  
cloud aerosol properties (Meyer et al., 2015; Painemal et al., 2020; Chang et al., 2021), and  
aerosol perturbations of  $N_c$  (Quaas et al., 2020). Factors that frequently result in biases in MODIS  
retrievals of cloud properties include subpixel heterogeneity (Zhang and Platnick, 2011), solar  
and satellite viewing geometry (Grosvenor and Wood, 2014; Painemal et al., 2021), cloud  
495 thermodynamic phase (Ahn et al., 2018), and drizzle occurrence (Zinner et al., 2010; Sinclair et  
al., 2021). These factors had limited impact on MODIS retrievals used in this study due to the low  
latitude of the ORACLES domain and observations of homogeneous, warm, closed cell marine  
stratocumulus over the southeast Atlantic with low precipitation rates (G21; G22).

Satellite estimates of  $N_c$  and aerosol perturbations of  $N_c$  over the southeast Atlantic have  
500 biases within 10 % of the in situ estimates. The differences between the MODIS and in situ  $R_e$  or





$\tau$  were reduced by screening data with MODIS  $R_e > 15 \mu\text{m}$  or MODIS  $\tau > 25$ , respectively. This is consistent with the improvement in correlations between MODIS  $N_c$  and in situ  $N_c$  from multiple field campaigns when using a threshold of maximum  $R_e$  of around  $15 \mu\text{m}$  (Gryspeerd et al., 2021). The MODIS-based screening led to MODIS estimates of aerosol-induced changes in  $N_c$ ,  $R_e$ , and  $\tau$  within  $5 \text{ cm}^{-3}$ ,  $0.5 \mu\text{m}$ , and  $0.7$  of the in situ estimates. Agreement between the MODIS and in situ estimates of aerosol-induced changes in  $N_c$ ,  $R_e$ , and  $\tau$  was associated with consistent biases in MODIS retrievals of cloud properties across different aerosol regimes. Such agreement suggests cloud properties for horizontally homogeneous, warm, closed cell marine stratocumulus can be estimated using MODIS retrievals in the absence of in situ datasets.

Better accuracy in remote sensing retrievals of the aerosol layer is needed to constrain the uncertainties in satellite estimates of  $\text{RF}_{\text{aci}}$  over the southeast Atlantic (Douglas and L'Ecuyer, 2020). In particular, biases in satellite estimates of the placement or optical and microphysical properties of the above-cloud aerosol layer need to be addressed (Rajapakshe et al., 2017; Painemal et al., 2020; Peers et al., 2021). The High Spectral Resolution Lidar Generation 2 (HSRL-2) (Hair et al., 2008) was used to measure aerosol extinction and backscatter at 355, 532, and 1064 nm during all three ORACLES campaigns. Research is ongoing to use HSRL-2 data for estimating the vertical profile of cloud condensation nuclei (Lenhardt, 2021). Accounting for the attenuation of upwelling solar radiation by above-cloud absorbing aerosols over the southeast Atlantic could increase the average MODIS  $\tau$  and  $R_e$  by up to 9 % and 2 %, respectively (Meyer et al., 2015). The Research Scanning Polarimeter (RSP) (Cairns et al., 1999) was used during ORACLES to collect polarimetric retrievals of cloud properties (Alexandrov et al., 2012) which do not operate under the assumptions required for MODIS retrievals. RSP retrievals can help examine



biases in MODIS retrievals of clouds with higher precipitation rates or bimodal size distributions (Sinclair et al., 2021; Fu et al., 2022) or complicated solar and viewing geometry (e.g., Painemal et al., 2021). Future work will use RSP retrievals combined with other airborne datasets to evaluate MODIS retrievals while accounting for above-cloud aerosols (e.g., Chang et al., 2021).

## 6 Conclusions

In situ measurements of  $N_c$ ,  $R_e$ , and  $\tau$  for marine stratocumulus over the southeast Atlantic were collected during the NASA ORACLES field campaign. In situ data from 145 cloud profiles were co-located with MODIS retrievals from the Terra and Aqua satellites with  $\Delta T$  less than 1 hour. The average MODIS  $R_e$  and  $\tau$  (11.3  $\mu\text{m}$  and 11.7) were greater than the average in situ  $R_e$  and  $\tau$  (9.7  $\mu\text{m}$  and 9.4) with  $R = 0.77$  and 0.73, respectively. The average bias in MODIS  $R_e$  was  $1.6 \pm 1.8 \mu\text{m}$  and the average bias in MODIS  $\tau$  was  $2.3 \pm 3.4$ , where the uncertainty represents the sum of the average MODIS retrieval uncertainty and the in situ measurement uncertainty.

MODIS  $N_c$  (151  $\text{cm}^{-3}$ ) had an estimated calculation error of 30.5 % and showed good agreement with in situ  $N_c$  (151  $\text{cm}^{-3}$ ) with  $R = 0.90$  and an average bias of  $0 \pm 64 \text{ cm}^{-3}$ . The retrieval uncertainty for MODIS  $R_e$  provided the largest source of error in calculating MODIS  $N_c$  but compensating uncertainties for  $\tau$ ,  $k$ ,  $C_w$ , and  $\alpha$  resulted in good agreement. Cloud profiles with an  $N_c$  bias greater than 50  $\text{cm}^{-3}$  were associated with higher variability in the in situ  $N_c$ . The biases in MODIS  $R_e$  and  $\tau$  were lower for lower bounds of  $\Delta T$  and for retrievals from MODIS Terra compared to MODIS Aqua. Profiles with MODIS  $R_e > 15 \mu\text{m}$  had larger biases in MODIS  $R_e$  (average bias = 4.5  $\mu\text{m}$ ) and profiles with MODIS  $\tau > 25$  had larger biases in MODIS  $\tau$  (average bias = 8.1).



Variability in the vertical profile of absorbing aerosols over the southeast Atlantic was associated with changes in  $N_c$ ,  $R_e$ , and  $\tau$  under similar meteorological conditions. There were 67  
545 “contact” profiles where  $N_a > 500 \text{ cm}^{-3}$  was sampled within 100 m above cloud tops while 78  
“separated” profiles had  $N_a < 500 \text{ cm}^{-3}$  up to 100 m above cloud tops. Contact profiles had higher  
in situ  $N_c$  and  $\tau$  ( $88 \text{ cm}^{-3}$  and 2.5 higher) and lower in situ  $R_e$  ( $2.2 \mu\text{m}$  lower) compared to separated  
profiles. MODIS retrievals were able to estimate the sign of these aerosol-induced changes in  $N_c$ ,  
 $R_e$ , and  $\tau$ . The magnitude of the MODIS estimates of differences between contact and separated  
550 profiles was within  $5 \text{ cm}^{-3}$ ,  $0.5$ , and  $0.2 \mu\text{m}$  of the in situ estimates when profiles with MODIS  $R_e$   
>  $15 \mu\text{m}$  or MODIS  $\tau > 25$  were removed.

The agreement between MODIS and in situ estimates of aerosol-induced changes in cloud  
microphysical properties over the southeast Atlantic was associated with similar biases in MODIS  
retrievals across different aerosol conditions. This motivates the use of MODIS retrievals to study  
555 ACI for homogeneous marine stratocumulus over a larger domain of the southeast Atlantic and  
over longer timescales than is possible using in situ data. Future work will be aimed at improving  
lidar and polarimetric retrievals of the vertical profile and microphysical and optical properties of  
absorbing aerosols over the southeast Atlantic layers and the underlying cloud properties (Zeng  
et al., 2014; Rajapakshe et al., 2017; Painemal et al., 2020; Lenhardt, 2021).

#### 560 **APPENDIX A – Scaling the CAS/CDP $n(D)$ based on King LWC**

For ORACLES 2016, CAS data were used in the analysis since CDP measurements were  
invalid due to an instrument misalignment issue. G22 showed there were statistically significant  
differences between the average CAS LWC of  $0.15 \pm 0.09 \text{ g m}^{-3}$  ( $\pm$  one standard deviation) and



the average King LWC of  $0.28 \pm 0.15 \text{ g m}^{-3}$  ( $R = 0.80$ ). The LWC comparison provides an estimate  
565 of the uncertainties in the CAS data due to known issues like coincidence of particles in the  
sample volume (Lance et al., 2012) and uncertainties in the collection geometry (e.g.,  
Baumgardner et al., 2017). Comparisons between CAS and CDP  $N_c$  (when CDP data were  
available) indicate the CAS may be affected by coincidence of particles within the sample volume.  
However, accounting for coincidence while processing the CAS data affected  $N_c$  by less than 2 %.  
570 Based on a recommendation by the manufacturers of CAS (Droplet Measurement Technologies,  
DMT), a sample area of  $0.26 \text{ mm}^2$  was used to process CAS droplet counts to obtain  $N_c$  instead of  
using  $0.13 \text{ mm}^2$  from the CAS manual.

For the six flights selected for analysis, the King LWC and CAS LWC had a best fit slope ( $a$ )  
between 0.46 and 0.63 and  $R = 0.71$  to 0.93 (Table A1). Therefore, an adjustment is used to  
575 increase the CAS LWC to match King LWC. The simplest way to do this would be to increase the  
CAS sample area, which is a first order adjustment that assumes the CAS is sizing the droplets  
correctly. However, based on the LWC differences, it is hypothesized the CAS was under-sizing  
the droplets passing through the CAS sample volume. The methodology outlined by PZ11 was  
thus used to account for the sizing bias wherein the CAS  $n(D)$  was scaled by adjusting the CAS size  
580 bins using the King LWC as a reference by setting

$$\text{CAS LWC} = a \times \text{King LWC} . \quad (\text{A1})$$

The scaled midpoint diameter for the  $i^{\text{th}}$  CAS size bin ( $D_i^*$ ) is determined as

$$D_i^* = a^{-1/3} D_i , \quad (\text{A2})$$



where  $D_i$  is the midpoint diameter for the  $i^{\text{th}}$  CAS size bin. The  $D_i$  used to calculate the CAS  $R_e$  and  
585 LWC is replaced by  $D_i^*$  to calculate the scaled CAS  $R_e$  and LWC. The CAS size bin midpoints were  
thus increased (by up to 30 %) since  $D_i^* > D_i$  for  $a < 1$  and each flight had  $a < 1$ . The average in situ  
 $R_e$  for the 34 profiles from ORACLES 2016 with a co-located MODIS retrieval (Table 2) increased  
from 8.6  $\mu\text{m}$  for unscaled CAS  $n(D)$  to 10.6  $\mu\text{m}$  for CAS  $n(D)$  scaled using Eqs. (A1) and (A2).

The average MODIS  $R_e$  (12.4  $\mu\text{m}$ ) overestimated the average in situ  $R_e$  from both the  
590 unscaled and scaled CAS  $n(D)$ . When the CAS  $n(D)$  was scaled, the number of profiles having in  
situ  $R_e > \text{MODIS } R_e$  increased from 0 to 2 and the average  $\Delta R_e$  decreased from 3.8  $\mu\text{m}$  ( $R = 0.83$ )  
to 1.8  $\mu\text{m}$  ( $R = 0.86$ ), relative to using the unscaled CAS  $n(D)$ . These changes were consistent with  
the hypothesis of CAS under sizing the droplets passing through the CAS sample volume. Since  
the average  $\Delta R_e$  for scaled CAS  $n(D)$  was consistent with previous studies (PZ11; Painemal et al.,  
595 2021), the scaled CAS  $n(D)$  was used in the analysis.

Valid CDP measurements were available for ORACLES 2017 and 2018. For the research  
flights from ORACLES 2017 and 2018, the average CDP LWC was  $0.18 \pm 0.16 \text{ g m}^{-3}$  and  $0.21 \pm 0.14$   
 $\text{g m}^{-3}$ , the average King LWC was  $0.21 \pm 0.15 \text{ g m}^{-3}$  and  $0.20 \pm 0.12 \text{ g m}^{-3}$ , and the average CAS  
LWC was  $0.09 \pm 0.07 \text{ g m}^{-3}$  and  $0.10 \pm 0.07 \text{ g m}^{-3}$ , respectively (G22). The differences between the  
600 King LWC and the CDP LWC are within the typical uncertainties of these in situ cloud probes  
(Baumgardner et al., 2017). Nevertheless, the impact of scaling the CDP data was investigated  
using Eqs. (A1) and (A2) to determine if this would lead to qualitative changes in the results.

For 14 out of 18 flights from ORACLES 2017 and 2018, the King LWC and CDP LWC had  $0.7$   
 $< a < 1.4$  and the CDP size bin midpoints were adjusted by less than 13 % following Eq. (A2). When



605 the CDP  $n(D)$  was scaled for the 42 profiles from ORACLES 2017, the average CDP  $R_e$  increased from 7.6  $\mu\text{m}$  to 8.7  $\mu\text{m}$ , the number of profiles having in situ  $R_e > \text{MODIS } R_e$  increased from 2 to 21, and the average  $\Delta R_e$  decreased from 1.4  $\mu\text{m}$  ( $R = 0.57$ ) to 0.3  $\mu\text{m}$  ( $R = 0.43$ ), relative to using the unscaled CDP  $n(D)$ . Scaling the CDP  $n(D)$  led to a decrease in the best fit slope for MODIS  $R_e$  as a function of in situ  $R_e$  (0.73 to 0.50) along with an increase in the intercept (3.5 to 4.7  $\mu\text{m}$ ).

610 These changes suggest the in situ  $R_e$  might be overestimated when the CDP  $n(D)$  is scaled, and the unscaled CDP  $n(D)$  was thus used in the study for ORACLES 2017. Given this and the closer agreement between CDP LWC and King LWC (compared to CAS LWC and King LWC), it is unlikely the CDP had a sizing bias like the CAS and thus the unscaled CDP  $n(D)$  was used in the analysis.

When the CDP  $n(D)$  was scaled for the 73 profiles from ORACLES 2018, the average CDP

615  $R_e$  increased from 10.5  $\mu\text{m}$  to 10.8  $\mu\text{m}$ , the number of profiles having in situ  $R_e > \text{MODIS } R_e$  increased from 9 to 15, and the average  $\Delta R_e$  decreased from 1.9  $\mu\text{m}$  ( $R = 0.68$ ) to 1.6  $\mu\text{m}$  ( $R = 0.62$ ), relative to using the unscaled CDP  $n(D)$ . The use of scaled CDP  $n(D)$  led to small changes in the best fit slope for MODIS  $R_e$  as a function of in situ  $R_e$  (0.77 to 0.73) and the intercept (4.3 to 4.5  $\mu\text{m}$ ). Scaling the CDP  $n(D)$  for ORACLES 2018 did not have a major impact on the CDP dataset.

620 To remain consistent with the use of unscaled CDP data for ORACLES 2017, unscaled CDP data were used in the study for ORACLES 2018, as well.

When MODIS  $R_e$  was compared with in situ  $R_e$  calculated using unscaled  $n(D)$  for all three campaigns, the average  $\Delta R_e$  was 2.2  $\mu\text{m}$  with  $R = 0.72$  and a best-fit slope and intercept of 0.86 and 3.5  $\mu\text{m}$ , respectively (Fig. A1a). In comparison, when MODIS  $R_e$  was compared with in situ  $R_e$

625 calculated using scaled  $n(D)$  for all three campaigns, the average  $\Delta R_e$  was 1.3  $\mu\text{m}$  with  $R = 0.70$



and a best-fit slope and intercept of 0.90 and 2.4  $\mu\text{m}$ , respectively (Fig. A1b). The use of either scaled or unscaled  $n(D)$  for all three campaigns did not lead to qualitative changes in the results presented in the study. MODIS  $R_e$  always had a positive bias greater than 1  $\mu\text{m}$  relative to in situ  $R_e$ . It must be noted that the quantitative changes highlight the uncertainties associated with in situ data which must be considered when validating satellite retrievals using airborne datasets (Witte et al., 2018).

#### Appendix B - In situ Measurement Uncertainties

The error for in situ measurements of  $N_c$ ,  $R_e$ , and  $\tau$  depend on droplet sizing and concentration uncertainties associated with limitations of instrument measurement principles and data processing algorithms (Baumgardner et al., 2017; McFarquhar et al., 2017). Although sources of in situ measurement uncertainty are relatively well known, there is no established methodology for calculating sizing and concentration uncertainties or propagating uncertainties to the error for in situ  $N_c$ ,  $R_e$ , or  $\tau$ . A single probe is unable to characterize the entire spectrum of cloud droplets, and droplet size distributions are derived by combining number distribution function from scattering and imaging probes (G22). This complicates uncertainty estimation and error propagation for in situ measurements. After accounting for instrument and data processing uncertainties, droplet sizing and concentration uncertainties can be  $\pm 20\%$  and  $\pm 50\%$  for imaging probes and  $\pm 50\%$  and  $\pm 20\%$  for scattering probes (Baumgardner et al., 2017).

Three approaches are examined for estimating the error for in situ  $N_c$ ,  $R_e$ , and  $\tau$ . First, sizing and concentration uncertainties of 10% each are assumed throughout the size distribution (Baumgardner et al., 2017) to derive a minimum estimate of the error. Second, uncertainties are



estimated based on inter-comparisons between cloud probes with similar measurement size ranges. Third, the standard error of the mean, defined as the standard deviation divided by the square root of the sample size, is calculated. For each variable, the maximum estimate out of the  
650 three approaches is designated as the error estimate.

For the first approach, the droplet concentration ( $N_c$ ) uncertainty is 10 %. Sizing and concentration uncertainties are not always independent, and Gaussian error propagation can underestimate the error. Thus, error ( $\delta$ ) in  $R_e$  and  $\tau$  is determined using the maxima and minima concentration and size as

$$655 \quad \delta x = \frac{x(D+\delta D, N(D)+\delta N(D)) - x(D-\delta D, N(D)-\delta N(D))}{2}, \quad x = \{\tau, R_e\} \quad (\text{B1})$$

where  $\delta D = 0.1 D$  and  $\delta N(D) = 0.1 N(D)$ .

Following Eq. (3),  $\delta \tau$  equals 0.3  $\tau$  and  $\delta R_e$  equals 0.1  $R_e$ . The fractional estimate for  $\delta \tau$  is greater than the equivalent estimate from Gaussian error propagation (0.22  $\tau$ ) while the estimate for  $\delta R_e$  is equivalent to the Gaussian error estimate. Following this approach, the average in situ  
660  $N_c$ ,  $R_e$ , and  $\tau$  error estimates are 15  $\text{cm}^{-3}$ , 1.0  $\mu\text{m}$ , and 2.8, respectively. For the second approach, average values of  $N_c$ ,  $R_e$ , and  $\tau$  from the scaled CAS datasets (Appendix A) are compared with the PDI dataset for ORACLES 2016 and with the CDP datasets for ORACLES 2017 and 2018 based on data availability (G22). Across deployments, the relative difference between  $N_c$ ,  $R_e$ , and  $\tau$  from the cloud probes was within 12.5 %, 10 %, and 21 %, respectively. Thus, the average in situ  $N_c$ ,  
665  $R_e$ , and  $\tau$  error estimates are 19  $\text{cm}^{-3}$ , 1.0  $\mu\text{m}$ , and 2.0, respectively. For the third approach, the standard deviation is divided by the square root of the sample size to determine the standard error of the mean. The  $N_c$ ,  $R_e$ , and  $\tau$  error estimates are 7.4  $\text{cm}^{-3}$ , 0.2  $\mu\text{m}$ , and 0.5, respectively.





Using the highest error estimate out of the three approaches, the average in situ  $N_c$ ,  $R_e$ , and  $\tau$  along with the error estimate are  $150 \pm 19 \text{ cm}^{-3}$ ,  $9.7 \pm 1.0 \text{ }\mu\text{m}$ , and  $9.4 \pm 2.8$ , respectively.

670 Uncertainty estimates for biases in MODIS retrievals relative to in situ measurements (Section 3) are defined as the sum of the retrieval uncertainty and calculation error for MODIS  $N_c$ ,  $R_e$  and  $\tau$ , and the in situ measurement uncertainty. The average MODIS  $N_c$  was  $150 \pm 45 \text{ cm}^{-3}$  and the bias in MODIS  $N_c$  was  $0 \pm 64 \text{ cm}^{-3}$ . The average MODIS  $R_e$  was  $11.3 \pm 0.8 \text{ }\mu\text{m}$  and the bias in MODIS  $R_e$  was  $1.6 \pm 1.8 \text{ }\mu\text{m}$ . The average MODIS  $\tau$  was  $11.7 \pm 0.6$  and the bias in MODIS  $\tau$  was  $2.3 \pm 3.4$ . The

675 average biases in MODIS retrievals relative to in situ measurements were within the MODIS retrieval and in situ measurement uncertainty for all three variables.

*Code availability.* University of Illinois/Oklahoma Optical Array Probe (OAP) Processing Software is available at <https://doi.org/10.5281/zenodo.1285969> (McFarquhar et al., 2018). The Airborne Data Processing and Analysis software package is available at

680 <https://doi.org/10.5281/zenodo.3733448> (Delene et al., 2020).

*Data availability.* All ORACLES data are accessible via digital object identifiers (DOIs) under the references: [https://doi.org/10.5067/Suborbital/ORACLES/P3/2018\\_V2](https://doi.org/10.5067/Suborbital/ORACLES/P3/2018_V2) (ORACLES Science Team, 2020a), [https://doi.org/10.5067/Suborbital/ORACLES/P3/2017\\_V2](https://doi.org/10.5067/Suborbital/ORACLES/P3/2017_V2) (ORACLES Science Team, 2020b), [https://doi.org/10.5067/Suborbital/ORACLES/P3/2016\\_V2](https://doi.org/10.5067/Suborbital/ORACLES/P3/2016_V2) (ORACLES Science Team,

685 2020c). The MODIS Collection 6 Cloud product is available at [dx.doi.org/10.5067/MODIS/MOD06\\_L2.061](https://dx.doi.org/10.5067/MODIS/MOD06_L2.061) (Platnick et al., 2017a, last access: May 26, 2022).

*Author contributions.* SG designed the study and analyzed the data with guidance from GMM and inputs from IYC, LG, FX, and JR. JRO'B, DJD, and MRP processed the cloud probe and PCASP data.



690 SG processed 2D-S and HVPS-3 data. All authors were involved with the ORACLES field campaign.  
GMM, MRP, and JR acquired funding. SG wrote the manuscript with guidance from GMM and  
reviews from all co-authors.

*Competing interests.* The authors declare that they have no conflicts of interest.

695 *Special issue statement.* This article is part of the special issue “New observations and related  
modeling studies of the aerosol–cloud–climate system in the Southeast Atlantic and southern  
Africa regions (ACP/AMT inter-journal SI)”. It is not associated with a conference.

700 *Acknowledgements.* We acknowledge the entire ORACLES science team for their contributions  
during data acquisition and analysis. We thank the NASA Ames Earth Science Project Office and  
the NASA P-3B crew for logistical and aircraft support. Some of the computing for this project  
was performed at the OU Supercomputing Center for Education & Research (OSCER) at the  
University of Oklahoma (OU).

*Financial support.* Funding for this project was obtained from NASA Award #80NSSC18K0222.  
ORACLES is funded by NASA Earth Venture Suborbital-2 grant NNH13ZDA001N-EVS2. SG was  
supported by NASA headquarters under the NASA Earth and Space Science Fellowship grants  
NNX15AF93G and NNX16A018H and by 80NSSC18K0222.

705



710 Table 1: List of research flights analyzed and the time range, number, sampling duration (in  
 gap ( $\Delta T$ ) less than 3600 s. Number and duration listed for profiles classified by above-cloud  
 aerosol location.

Flight Date	Time (UTC)	Separated	Contact	$Z_T$ (m)
06 Sep 2016	09:36 – 12:35	6 (256 s)	9 (606 s)	509 - 1002
10 Sep 2016	10:08 – 12:36	5 (255 s)	0 (0 s)	1151 - 1201
14 Sep 2016	09:36 – 13:02	3 (148 s)	0 (0 s)	635 - 814
20 Sep 2016	12:57 – 13:11	0 (0 s)	2 (61 s)	580 - 583
25 Sep 2016	11:00 – 13:51	6 (363 s)	3 (148 s)	729 - 1124
12 Aug 2017	11:53 – 13:46	0 (0 s)	8 (327 s)	1148 - 1193
13 Aug 2017	10:15 – 11:33	0 (0 s)	15 (718 s)	1334 - 1384
15 Aug 2017	12:55 – 13:27	0 (0 s)	6 (169 s)	1108 - 1148
21 Aug 2017	13:34 – 13:35	1 (18 s)	0 (0 s)	1447
24 Aug 2017	12:39 – 12:40	0 (0 s)	1 (10 s)	1099
28 Aug 2017	11:46 – 13:18	4 (168 s)	7 (496 s)	1070 - 1230
27 Sep 2018	10:07 – 13:11	10 (366 s)	0 (0 s)	819 - 1169
30 Sep 2018	09:50 – 12:24	6 (183 s)	7 (337 s)	747 - 840
03 Oct 2018	13:29 – 13:30	1 (13 s)	0 (0 s)	1157
07 Oct 2018	11:03 – 11:14	0 (0 s)	3 (136 s)	845 - 928
10 Oct 2018	10:16 – 13:31	2 (153 s)	1 (42 s)	991 - 1329
12 Oct 2018	13:12 – 14:19	3 (61 s)	0 (0 s)	1431 - 1905
15 Oct 2018	10:28 – 13:09	4 (125 s)	0 (0 s)	693 - 1547
19 Oct 2018	12:36 – 13:00	9 (661 s)	0 (0 s)	959 - 1276
21 Oct 2018	10:21 – 12.25	10 (504 s)	0 (0 s)	675 - 812
23 Oct 2018	10:28 – 13:08	8 (286 s)	5 (317 s)	873 - 1281
<b>Total (2016)</b>		<b>20 (1,022 s)</b>	<b>14 (815 s)</b>	
<b>Total (2017)</b>		<b>5 (186 s)</b>	<b>37 (1,720 s)</b>	
<b>Total (2018)</b>		<b>53 (2,352 s)</b>	<b>16 (832 s)</b>	
<b>Total</b>		<b>78 (3,560 s)</b>	<b>67 (3,367 s)</b>	

715 Table 2: Number of cloud profiles during ORACLES deployments with a co-located MODIS Terra  
 or Aqua retrieval for  $\Delta T$  less than 3600, 1800, or 900 s.

$\Delta T$	Terra (2016, 2017, 2018)	Aqua (2016, 2017, 2018)	Total
3600 s	20, 15, 39	14, 27, 30	145
1800 s	9, 3, 17	12, 13, 12	66
900 s	9, 1, 10	8, 7, 7	42



Table 3: Average bias ( $\Delta$ ), root mean square error (RMSE), and Pearson's correlation coefficient ( $R$ ) for MODIS (Terra, Aqua, combined) retrievals relative to in situ  $R_e$ ,  $\tau$ , and  $N_c$  for different  $\Delta T$ .

Parameter	$\Delta T$ (s)	Terra $\Delta$ , RMSE ( $R$ )	Aqua $\Delta$ , RMSE ( $R$ )	Combined $\Delta$ , RMSE ( $R$ )
$R_e$ ( $\mu\text{m}$ )	3600	1.5, 2.1 (0.82)	1.8, 2.9 (0.75)	1.6, 2.5 (0.77)
	1800	1.4, 1.5 (0.95)	2.1, 3.2 (0.78)	1.8, 2.6 (0.81)
	900	1.3, 1.5 (0.91)	1.8, 2.8 (0.81)	1.6, 2.3 (0.83)
$\tau$	3600	2.8, 6.1 (0.70)	1.9, 4.2 (0.73)	2.3, 5.2 (0.73)
	1800	1.7, 5.0 (0.90)	1.8, 4.0 (0.72)	1.8, 4.5 (0.85)
	900	1.3, 5.1 (0.91)	1.6, 4.5 (0.51)	1.4, 4.8 (0.86)
$N_c$ ( $\text{cm}^{-3}$ )	3600	0, 42 (0.87)	-1, 32 (0.93)	0, 38 (0.90)
	1800	11, 53 (0.82)	4, 32 (0.95)	7, 43 (0.90)
	900	9, 57 (0.74)	10, 34 (0.96)	10, 46 (0.87)

720 Table 4: Differences between the average  $R_e$ ,  $\tau$ , and  $N_c$  for contact and separated profiles based on MODIS retrievals (Terra, Aqua, and combined) and in situ measurements. Positive values indicate contact profiles had a higher value.

Parameter	$\Delta T$ (s)	Terra (In situ)	Aqua (In situ)	Combined (In situ)
$R_e$ ( $\mu\text{m}$ )	3600	-1.7 (-1.4)	-3.6 (-2.9)	-2.6 (-2.1)
	1800	-0.9 (-0.7)	-5.6 (-3.5)	-3.4 (-2.2)
	900	-0.3 (-0.4)	-5.9 (-3.5)	-3.1 (-2.0)
$\tau$	3600	6.0 (6.1)	-0.8 (-1.5)	3.0 (2.6)
	1800	7.1 (10.1)	-0.0 (-1.1)	2.4 (3.0)
	900	7.3 (10.5)	-2.6 (-3.1)	1.4 (2.6)
$N_c$ ( $\text{cm}^{-3}$ )	3600	83 (87)	115 (118)	99 (103)
	1800	80 (91)	153 (139)	113 (111)
	900	43 (77)	159 (131)	99 (102)

725 Table A1: ORACLES 2016 flight dates with the best fit slope ( $a$ ) and intercept ( $c$ ) between the average CAS LWC and King LWC from the flight.

Flight date	$a + c$ ( $R$ )
September 06	0.51 + 0.01 (0.71)
September 10	0.63 - 0.02 (0.93)
September 12	0.47 + 0.00 (0.88)
September 14	0.55 - 0.04 (0.85)
September 20	0.60 + 0.01 (0.88)
September 25	0.46 + 0.04 (0.74)

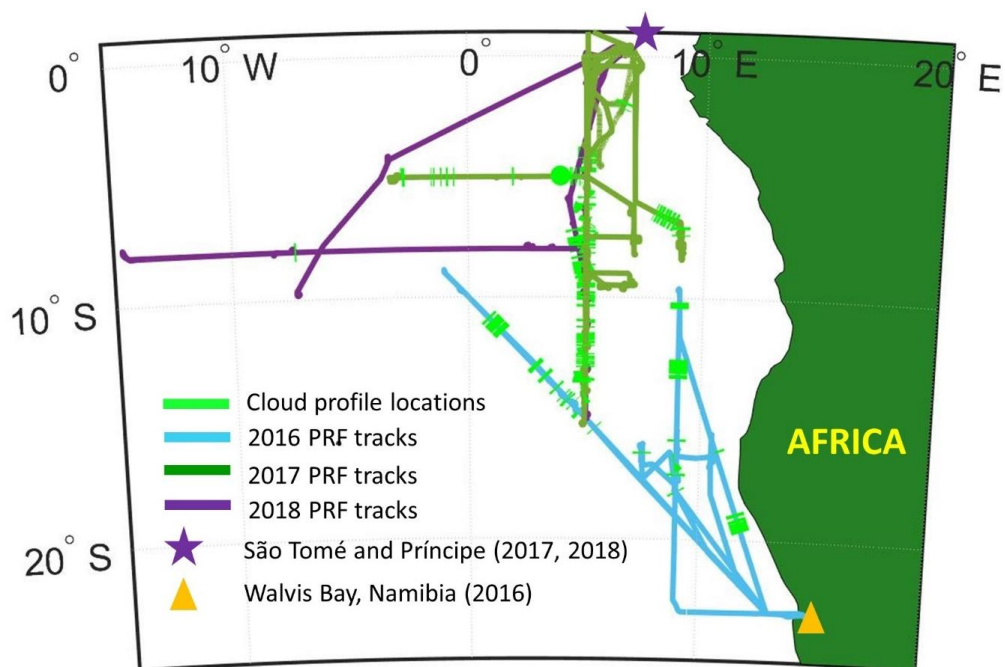
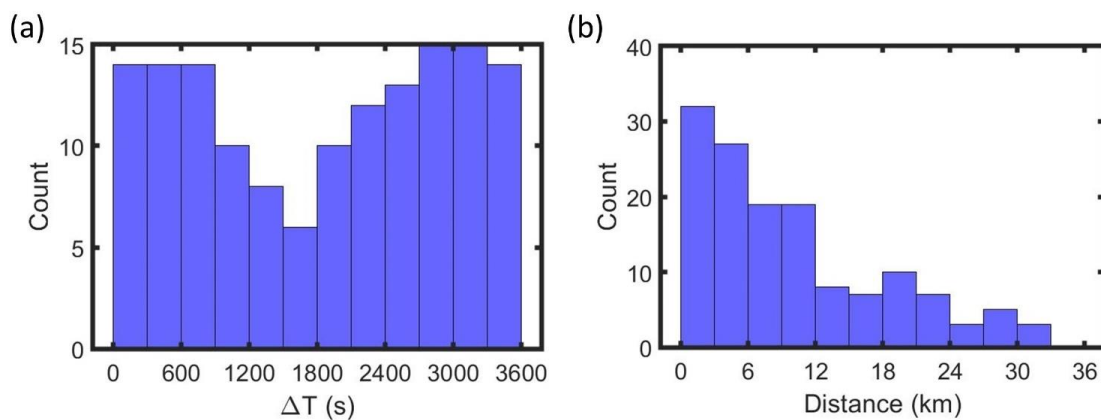
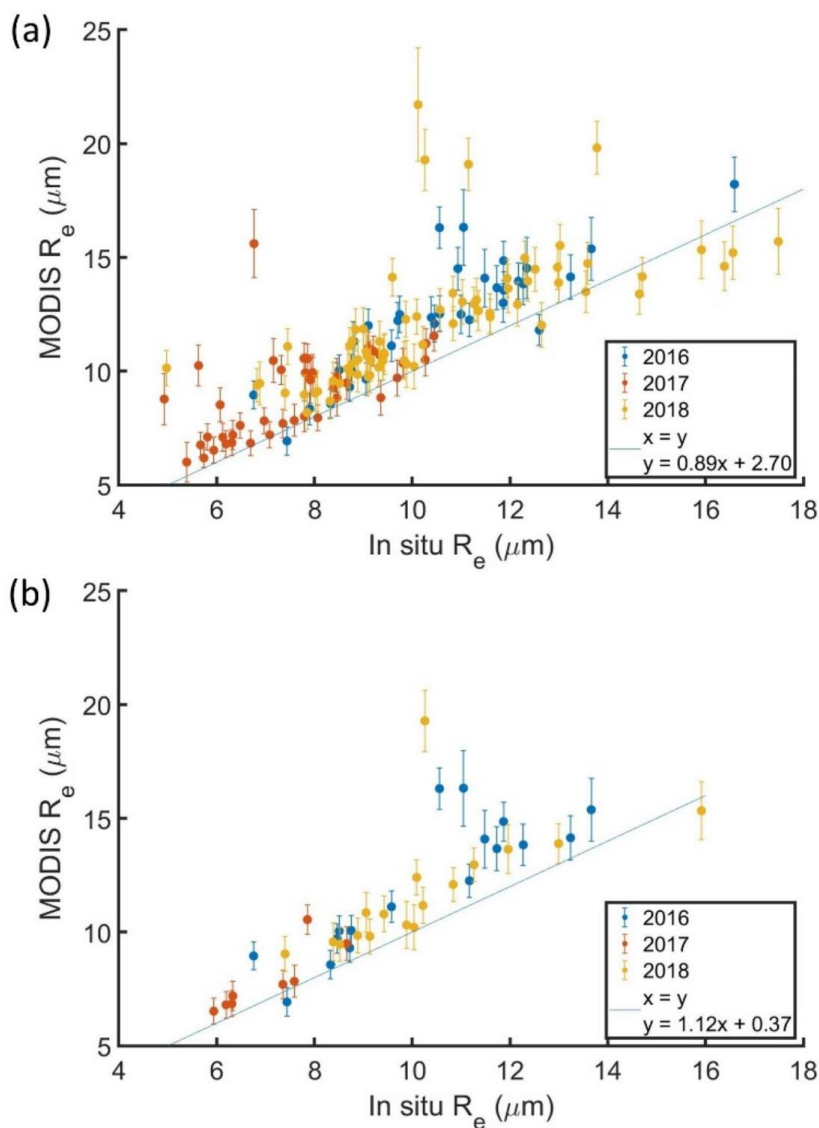


Figure 1: ORACLES flight tracks, base of operations, and sampling locations for profiles with a MODIS retrieval co-located with in situ data for  $\Delta T$  less than 3600 s.

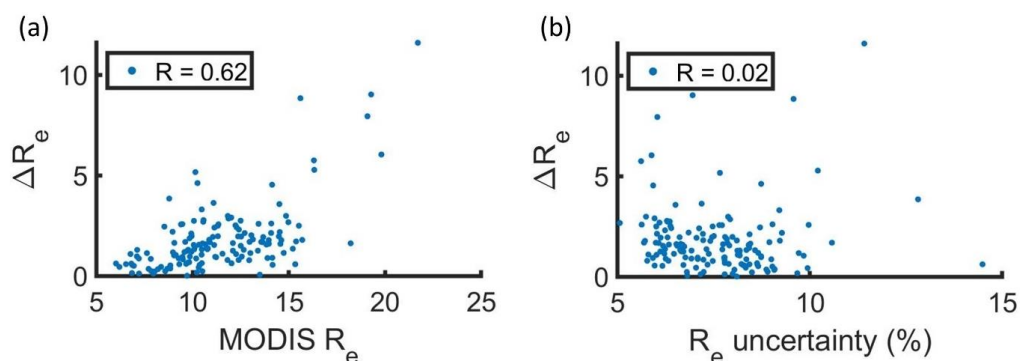


730

Figure 2: Histograms of (a) time gap between profiles and the co-located MODIS scan ( $\Delta T$ ) and (b) distance between profiles and the co-located MODIS pixel after adjusting for advection.



735 Figure 3: MODIS  $R_e$  versus in situ  $R_e$  for profiles with a MODIS retrieval co-located with in situ  
data for  $\Delta T$  (a) less than 3600 s and (b) less than 900 s colored by ORACLES deployment year.  
Each point represents a cloud profile with the in situ  $R_e$  averaged over the top 10 % of the cloud  
and MODIS  $R_e$  averaged over a 5 x 5 pixel domain.



740 Figure 4: Magnitude of the difference between MODIS  $R_e$  and in situ  $R_e$  ( $\Delta R_e$ ) for profiles with a MODIS retrieval co-located with in situ data for  $\Delta T$  less than 3600 s as a function of (a) MODIS  $R_e$  and (b) MODIS  $R_e$  uncertainty. Each point represents the average over a 5 x 5 pixel domain.

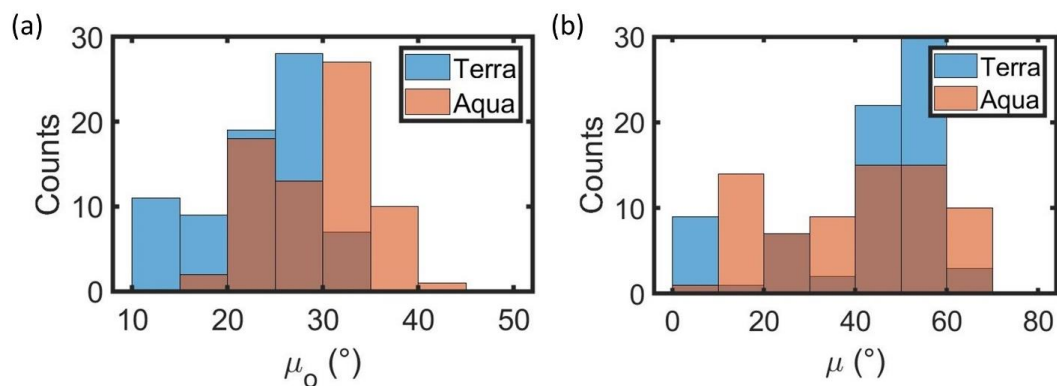
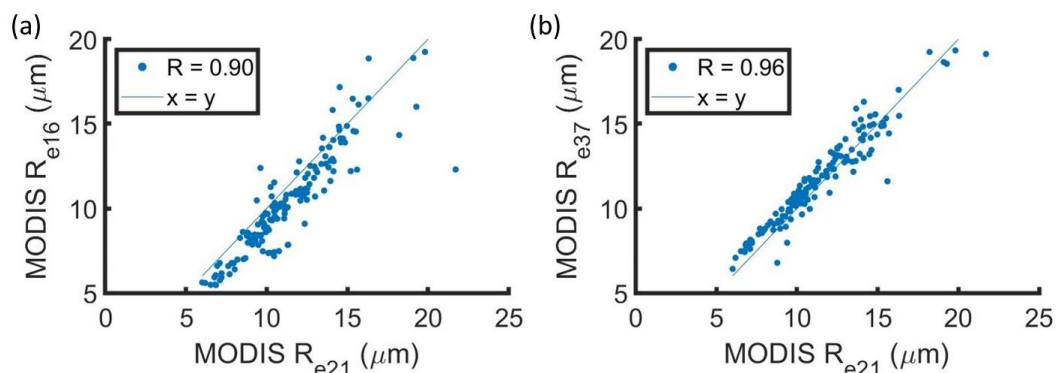
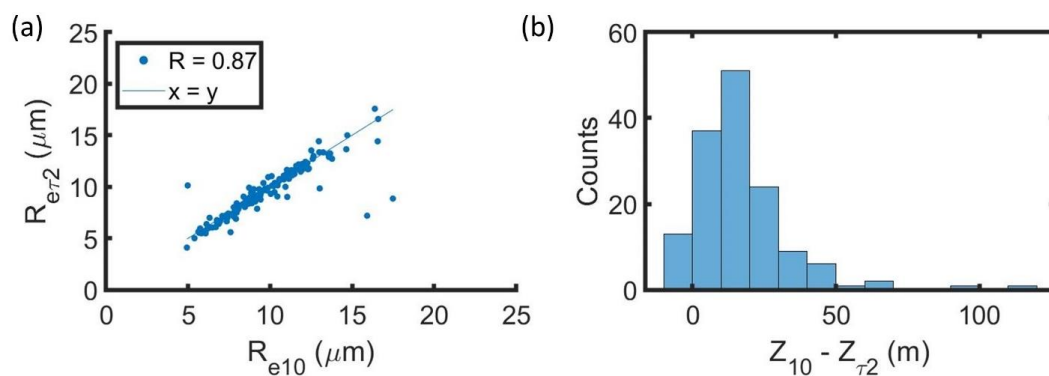


Figure 5: Histograms of (a) solar zenith angle ( $\mu_o$ ) and (b) sensor zenith angle ( $\mu$ ) for MODIS retrievals co-located with in situ data for  $\Delta T$  less than 3600 s.



745

Figure 6: (a)  $R_{e16}$  and (b)  $R_{e37}$  as a function of  $R_{e21}$  for MODIS retrievals co-located with in situ data for  $\Delta T$  less than 3600 s. Each point represents average values over a 5 x 5 pixel domain.



750 Figure 7: (a) Scatter between  $R_e$  at two optical depths below cloud top ( $R_{e\tau 2}$ ) versus  $R_e$  averaged over top 10 % of cloud layer ( $R_{e10}$ ) and (b) histogram of the difference between  $Z_{10}$  and  $Z_{\tau 2}$  for profiles with a MODIS retrieval co-located with in situ data for  $\Delta T$  less than 3600 s.



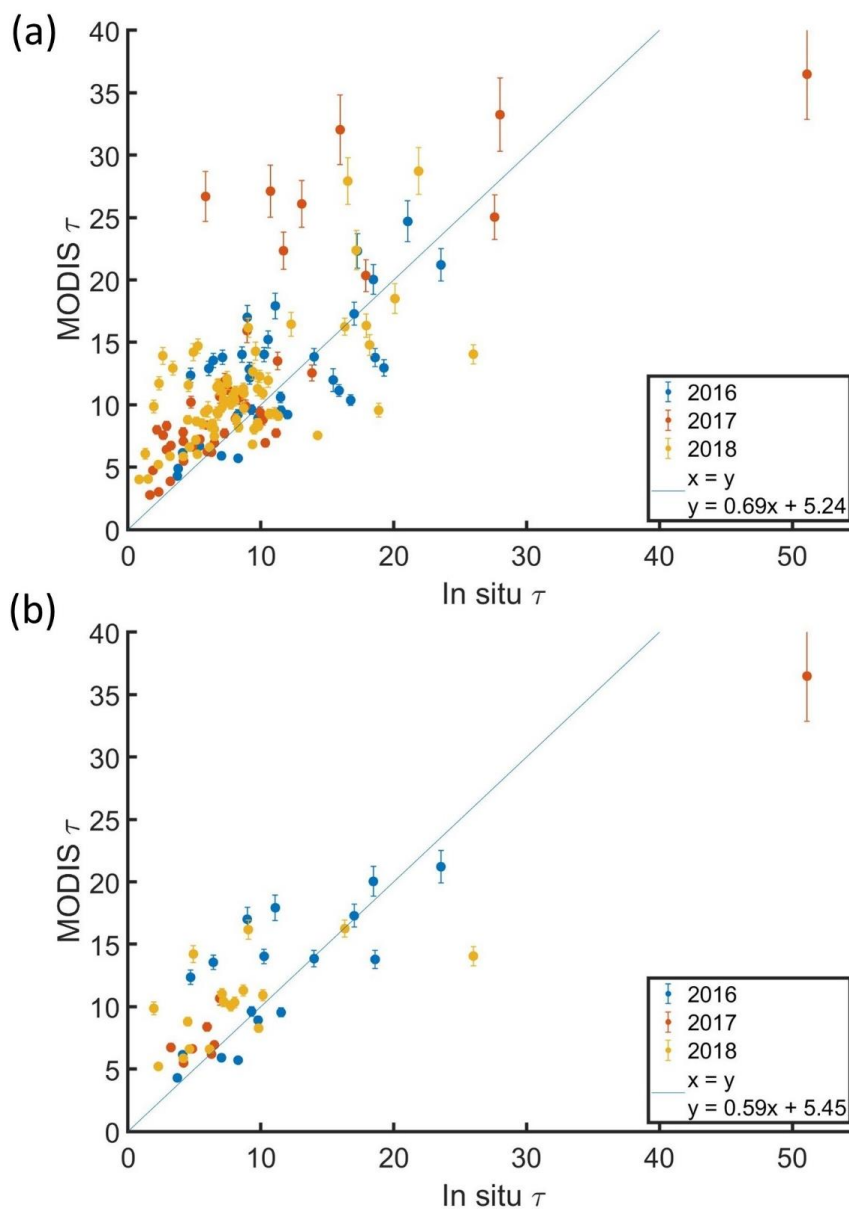


Figure 8: MODIS  $\tau$  versus in situ  $\tau$  for profiles with a MODIS retrieval co-located with in situ data for  $\Delta T$  (a) less than 3600 s and (b) less than 900 s colored by ORACLES deployment year. Each point represents a cloud profile with the MODIS  $\tau$  averaged over a 5 x 5 pixel domain.

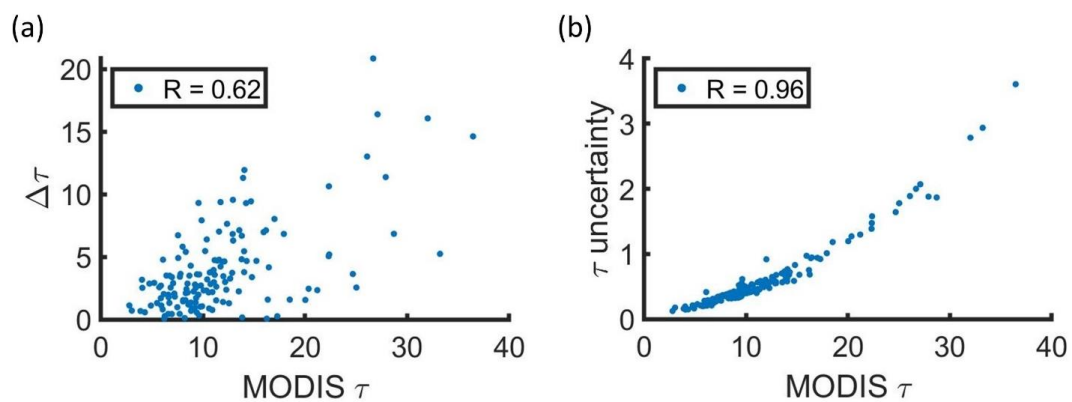
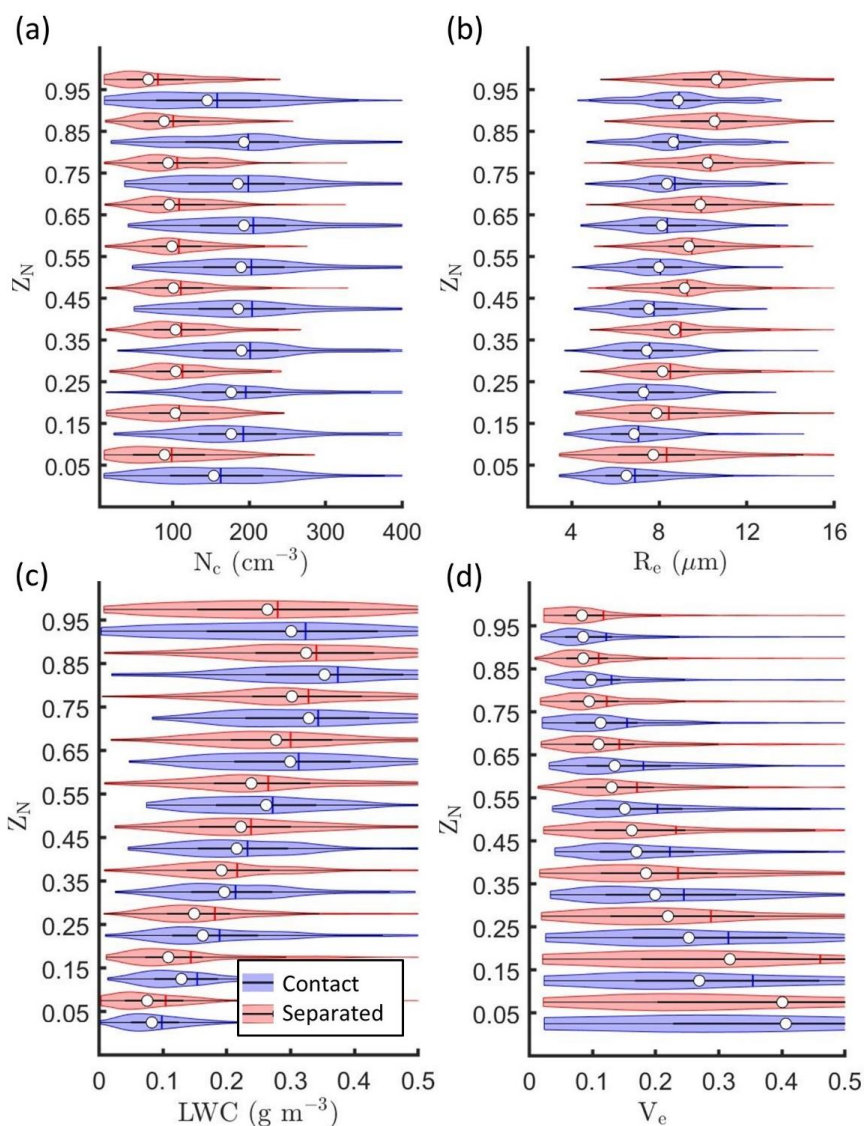
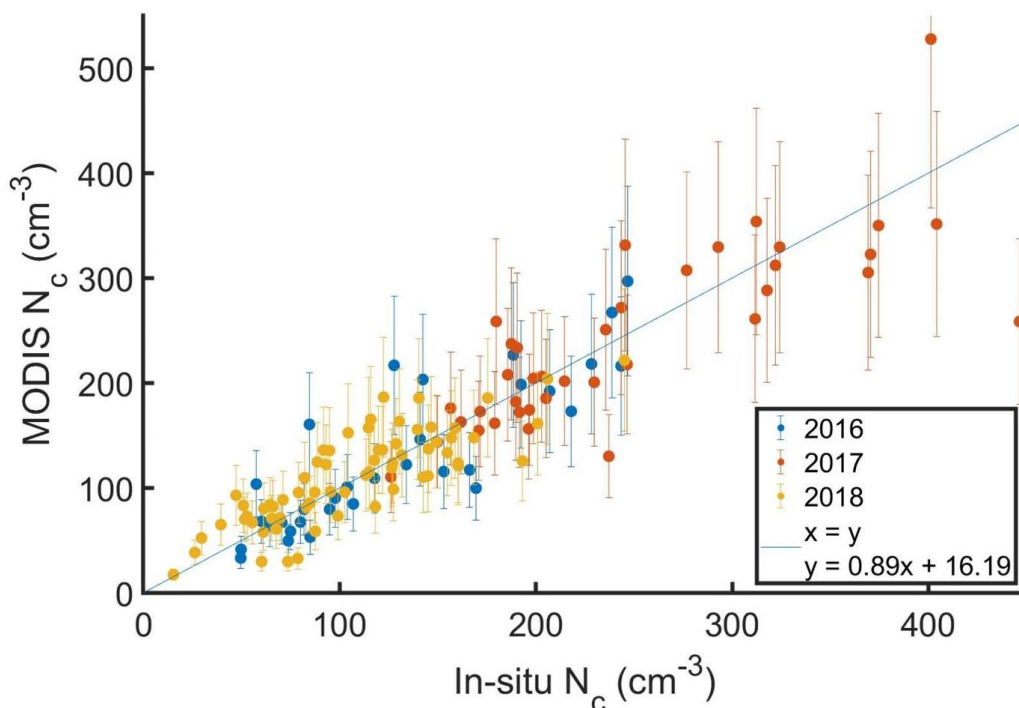


Figure 9: MODIS  $\tau$  versus (a) magnitude of the difference between MODIS  $\tau$  and in situ  $\tau$  ( $\Delta$ ) and (b) MODIS  $\tau$  retrieval uncertainty for profiles with a MODIS retrieval co-located with in situ data for  $\Delta T$  less than 3600 s. Each point represents average values over a 5 x 5 pixel domain.



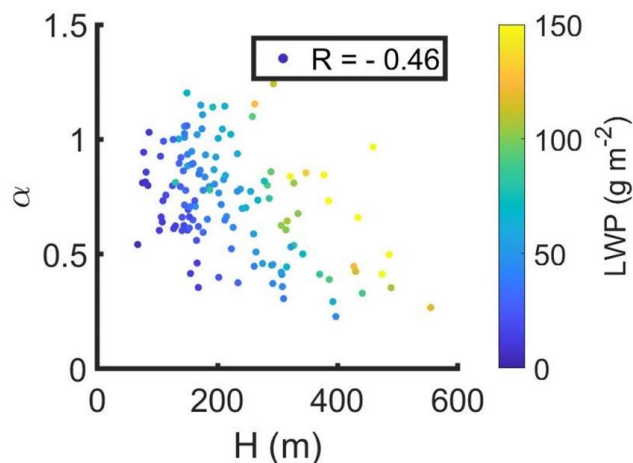
760

Figure 10: Kernel density estimates (indicated by width of shaded area) and boxplots showing mean (vertical line) and median (white circle) for (a)  $N_c$ , (b)  $R_e$ , (c) LWC, and (d)  $V_e$  versus normalized height in cloud ( $Z_N$ ) for profiles with a MODIS retrieval co-located with in situ data for  $\Delta T$  less than 3600 s.



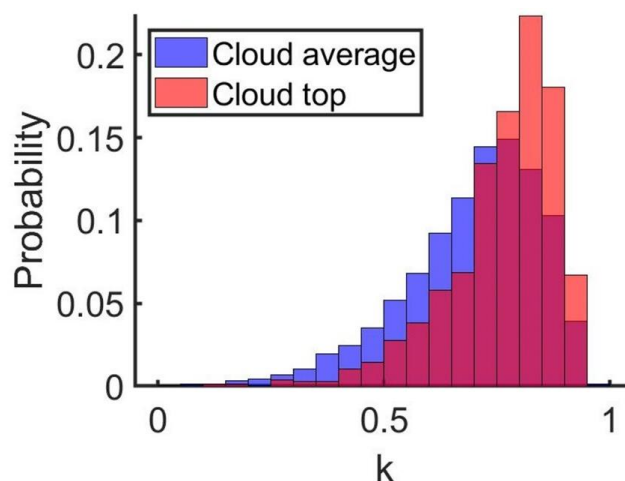
765

Figure 11: MODIS  $N_c$  versus in situ  $N_c$  for with a MODIS retrieval co-located with in situ data for  $\Delta T$  less than 3600 s colored by ORACLES deployment year. Each point represents a cloud profile with the in situ  $N_c$  averaged over the top half of the cloud and MODIS  $N_c$  calculated using MODIS  $R_e$  and  $\tau$  averaged over a 5 x 5 pixel domain.



770

Figure 12: Cloud adiabaticity ( $\alpha$ ) versus cloud thickness ( $H$ ) colored by liquid water path (LWP) for with a MODIS retrieval co-located with in situ data for  $\Delta T$  less than 3600 s.



775 Figure 13: Probability density function for  $k$  averaged over entire cloud layer (blue) or top 10 %  
of cloud (red) for profiles with a MODIS retrieval co-located with in situ data for  $\Delta T$  less than  
3600 s.

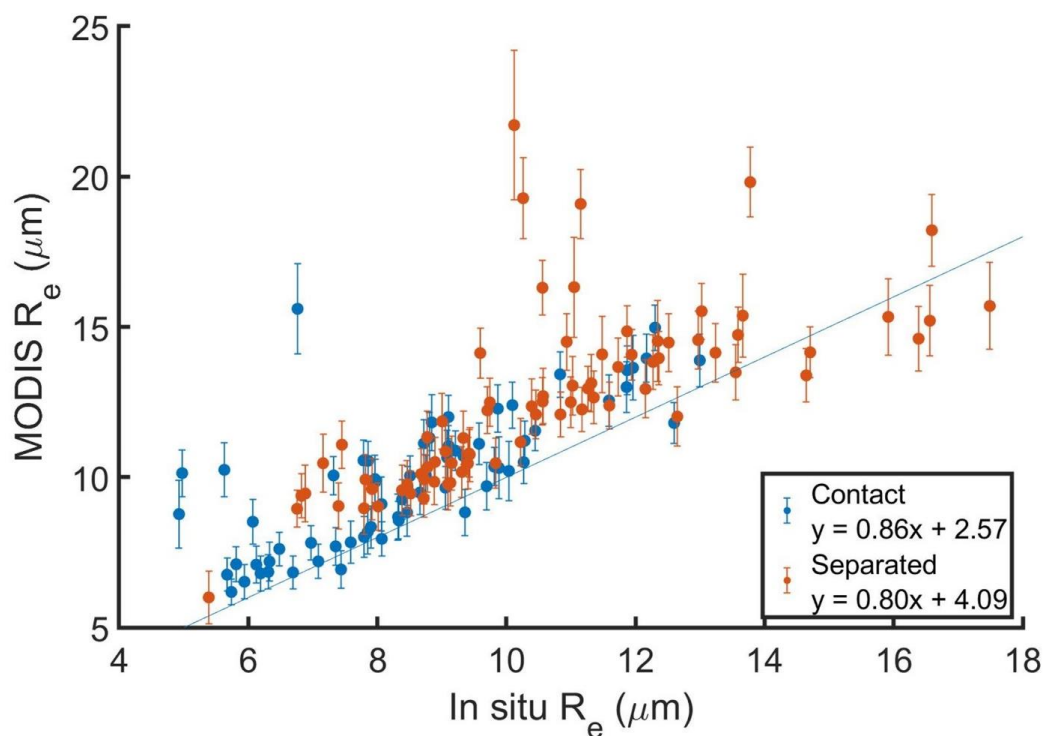
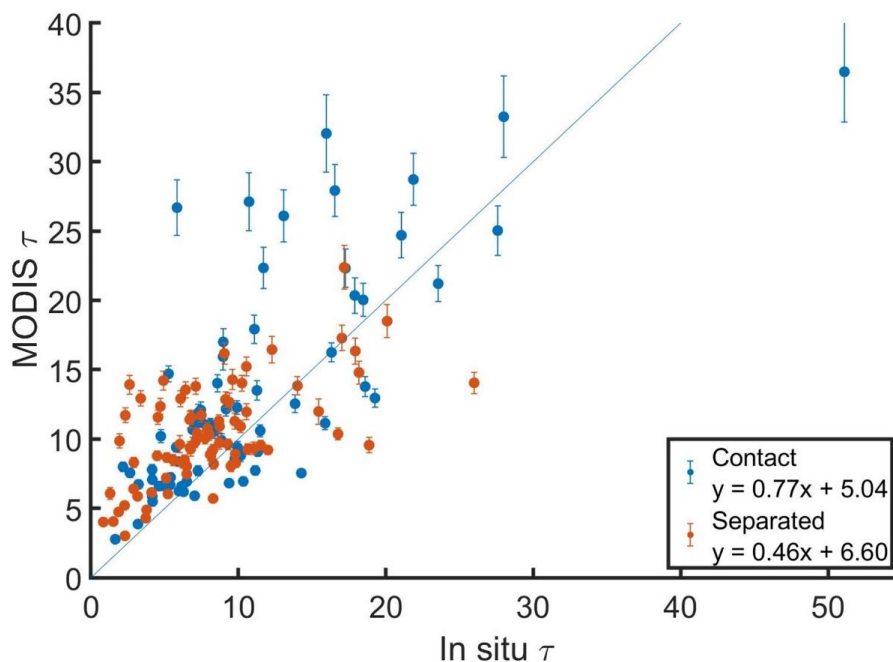


Figure 14: Same as Fig. 3a with cloud profiles colored based on regime classification.



780 Figure 15: Same as Fig. 8a with cloud profiles colored based on regime classification.

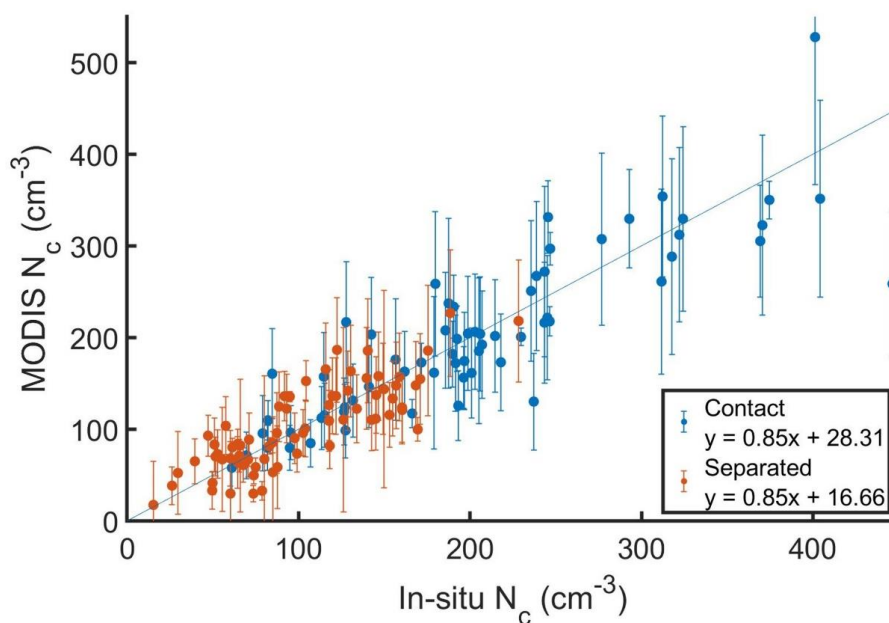
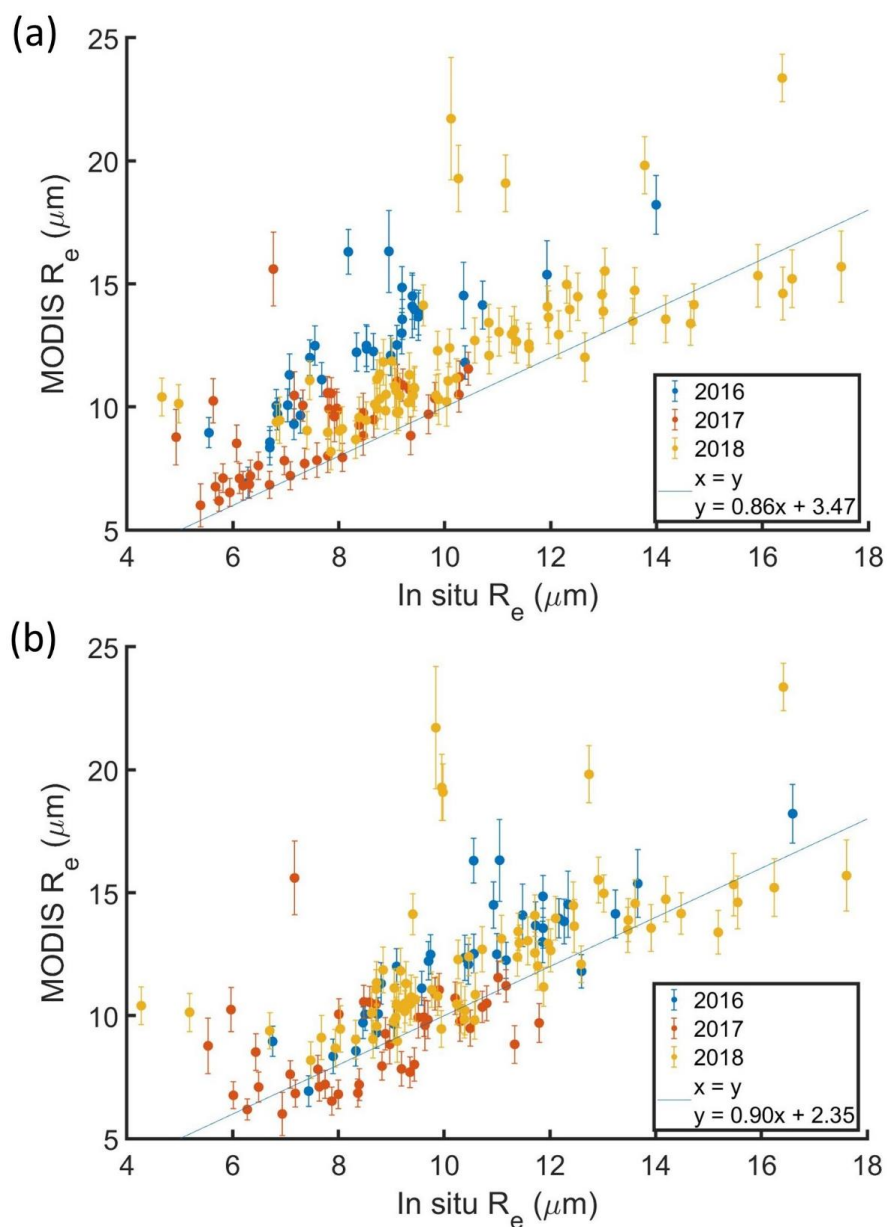


Figure 16: Same as Fig. 11 with cloud profiles colored based on regime classification.



785 Figure A1: Same as Fig. 3a with in situ  $R_e$  calculated (a) unscaled CAS and CDP  $n(D)$  and (b) CAS and CDP  $n(D)$  scaled based on King LWC.



## REFERENCES:

- 790 Adebisi, A. A. and Zuidema, P.: The role of the southern African easterly jet in modifying the  
southeast Atlantic aerosol and cloud environments, *Q. J. Roy. Meteor. Soc.*, 142, 1574–  
1589, <https://doi.org/10.1002/qj.2765>, 2016.
- Ahn, E., Huang, Y., Siems, S. T., and Manton, M. J.: A comparison of cloud microphysical properties  
derived from MODIS and CALIPSO with in situ measurements over the wintertime  
Southern Ocean, *J. Geophys. Res.-Atmos.*, 123, 11120–  
795 11140, <https://doi.org/10.1029/2018JD028535>, 2018.
- Albrecht, B.: Aerosols, Cloud Microphysics, and Fractional Cloudiness, *Science*, 245, 1227–1230,  
1989.
- Alexandrov, M. D., Cairns, B., Emde, C., Ackerman, A. S., and van Diedenhoven, B.: Accuracy  
assessments of cloud droplet size retrievals from polarized reflectance measurements by  
800 the research scanning polarimeter, *Remote Sens. Environ.*, 125, 92–  
111, <https://doi.org/10.1016/j.rse.2012.07.012>, 2012.
- Baumgardner, D., Abel, S. J., Axisa, D., Cotton, R., Crosier, J., Field, P., Gurganus, C., Heymsfield,  
A., Korolev, A., Kraemer, M., Lawson, P., McFarquhar, G., Ulanowski, Z., and Um, J.: Cloud  
ice properties: in situ measurement challenges, *Meteor. Monographs*, 58, 9.1–9.23,  
805 <https://doi.org/10.1175/AMSMONOGRAPHS-D-16-0011.1>, 2017.
- Baumgardner, D., Jonsson, H., Dawson, W., Connor, D. O., and Newton, R.: The cloud, aerosol  
and precipitation spectrometer (CAPS): A new instrument for cloud investigations, *Atmos.  
Res.*, 59, 59–60, 2001.





- Boucher, O., Randall, D., Artaxo, P., Bretherton, C., Feingold, G., Forster, P., Kerminen, V.-M.,  
810 Kondo, Y., Liao, H., Lohmann, U., Rasch, P., Satheesh, S. K., Sherwood, S., Stevens, B., and  
Zhang, X. Y.: Clouds and Aerosols. In: Climate Change 2013: The Physical Science Basis,  
Contribution of Working Group I to the Fifth Assessment Report of the Intergovernmental  
Panel on Climate Change, edited by: Stocker, T. F., Qin, D., Plattner, G.-K., Tignor, M.,  
Allen, S. K., Boschung, J., Nauels, A., Xia, Y., Bex, V., and Midgley, P. M., Cambridge  
815 University Press, Cambridge, United Kingdom and New York, NY, USA, 571–657, 2013.
- Braun, R. A., Dadashazar, H., MacDonald, A. B., Crosbie, E., Jonsson, H. H., Woods, R. K., Flagan,  
R. C., Seinfeld, J. H., and Sorooshian, A.: Cloud Adiabaticity and Its Relationship to Marine  
Stratocumulus Characteristics Over the Northeast Pacific Ocean, *J. Geophys. Res.-Atmos.*,  
123, 13790–13806, <https://doi.org/10.1029/2018JD029287>, 2018.
- 820 Brenguier, J.-L., Burnet, F., and Geoffroy, O.: Cloud optical thickness and liquid water path – does  
the  $k$  coefficient vary with droplet concentration?, *Atmos. Chem. Phys.*, 11, 9771–9786,  
<https://doi.org/10.5194/acp-11-9771-2011>, 2011.
- Brenguier, J.-L., Pawlowska, H., Schüller, L., Preusker, R., Fischer, J., and Fouquart, Y.: Radiative  
properties of boundary layer clouds: Droplet effective radius versus number  
825 concentration, *J. Atmos. Sci.*, 57, 803–821, 2000.
- Cai, Y., Snider, J. R., and Wechsler, P.: Calibration of the passive cavity aerosol spectrometer  
probe for airborne determination of the size distribution, *Atmos. Meas. Tech.*, 6, 2349–  
2358, <https://doi.org/10.5194/amt-6-2349-2013>, 2013.



- Chang, F.-L. and Li, Z.: Estimating the vertical variation of cloud droplet effective radius using  
830 multispectral near-infrared satellite measurements, *J. Geophys. Res.*, **107**, AAC 7-1–AAC  
7-12, <https://doi.org/10.1029/2001JD0007666>, 2002.
- Chang, I., Gao, L., Burton, S. P., Chen, H., Diamond, M., Ferrare, R. A., Flynn, C. J., Kacenelenbogen,  
M., LeBlanc, S. E., Meyer, K. G., Pistone, K., Schmidt, S., Segal-Rozenhaimer, M.,  
Shinozuka, Y., Wood, R., Zuidema, P., Redemann, J., and Christopher, S. A.:  
835 Spatiotemporal heterogeneity of aerosol and cloud properties over the southeast  
Atlantic: An observational analysis, *Geophys. Res. Lett.*, **48**,  
e2020GL091469, <https://doi.org/10.1029/2020GL091469>, 2021.
- Christensen, M. W., Chen, Y.-C., and Stephens, G. L.: Aerosol indirect effect dictated by liquid  
clouds, *J. Geophys. Res.-Atmos.*, **121**, 14636–14650,  
840 <https://doi.org/10.1002/2016JD025245>, 2016.
- Chuang, P. Y., Saw, E. W., Small, J. D., Shaw, R. A., Sipperley, C. M., Payne, G. A., and Bachalo, W.:  
Airborne Phase 495 Doppler Interferometry for Cloud Microphysical Measurements,  
*Aerosol Sci. Technol.*, **42**, 685–703, 2008.
- Cochrane, S. P., Schmidt, K. S., Chen, H., Pilewskie, P., Kittelman, S., Redemann, J., LeBlanc, S.,  
845 Pistone, K., Segal Rozenhaimer, M., Kacenelenbogen, M., Shinozuka, Y., Flynn, C., Ferrare,  
R., Burton, S., Hostetler, C., Mallet, M., and Zuidema, P.: Biomass burning aerosol heating  
rates from the ORACLES (ObseRvations of Aerosols above CLouds and their intEractionS)  
2016 and 2017 experiments, *Atmos. Meas. Tech.*, **15**, 61–77,  
<https://doi.org/10.5194/amt-15-61-2022>, 2022.



- 850 Das, S., Harshvardhan, H., & Colarco, P. R.: The influence of elevated smoke layers on stratocumulus clouds over the SE Atlantic in the NASA Goddard Earth Observing System (GEOS) model. *Journal of Geophysical Research: Atmospheres*, 125, e2019JD031209. <https://doi.org/10.1029/2019JD031209>, 2020.
- Delene, D. J.: Airborne Data Processing and Analysis Software Package, *Earth Sci. Inform.*, 4, 29–  
855 44, 2011.
- Douglas, A. and L'Ecuyer, T.: Quantifying cloud adjustments and the radiative forcing due to aerosol–cloud interactions in satellite observations of warm marine clouds, *Atmos. Chem. Phys.*, 20, 6225–6241, <https://doi.org/10.5194/acp-20-6225-2020>, 2020.
- Douglas, A. and L'Ecuyer, T.: Global evidence of aerosol-induced invigoration in marine cumulus  
860 clouds, *Atmos. Chem. Phys.*, 21, 15103–15114, <https://doi.org/10.5194/acp-21-15103-2021>, 2021.
- Formenti, P., D'Anna, B., Flamant, C., Mallet, M., Piketh, S. J., Schepanski, K., Waquet, F., Auriol, F., Brogniez, G., Burnet, F., Chaboureaud, J.-P., Chauvigné, A., Chazette, P., Denjean, C., Desboeufs, K., Doussin, J.-F., Elguindi, N., Feuerstein, S., Gaetani, M., Giorio, C., Klopper, D., Mallet, M. D., Nabat, P., Monod, A., Solmon, F., Namwoonde, A., Chikwililwa, C.,  
865 Mushi, R., Welton, E. J., and Holben, B.: The Aerosols, Radiation and Clouds in southern Africa (AEROCLO-sA) field campaign in Namibia: overview, illustrative observations and way forward, *B. Am. Meteorol. Soc.*, 100, 1277–1298, <https://doi.org/10.1175/BAMS-D-17-0278.1>, 2019.



870 Fu, D., Di Girolamo, L., Liang, L., & Zhao, G.: Regional biases in MODIS marine liquid water cloud  
drop effective radius deduced through fusion with MISR. *Journal of Geophysical Research:  
Atmospheres*, 124, 2019JD031063, 2019.

Fu, D., Di Girolamo, L., Rauber, R. M., McFarquhar, G. M., Nesbitt, S. W., Loveridge, J., Hong, Y.,  
van Diedenhoven, B., Cairns, B., Alexandrov, M. D., Lawson, P., Woods, S., Tanelli, S., Sy,  
875 O. O., Schmidt, S., Hostetler, C. A., and Scarino, A. J.: An evaluation of liquid cloud droplet  
effective radius derived from MODIS, airborne remote sensing and in situ measurements  
from CAMP<sup>2</sup>Ex, *Atmos. Chem. Phys. Discuss.* [preprint], <https://doi.org/10.5194/acp-2022-73>, in review, 2022.

Grosvenor, D. P. and Wood, R.: The effect of solar zenith angle on MODIS cloud optical and  
880 microphysical retrievals within marine liquid water clouds, *Atmos. Chem. Phys.*, 14, 7291–  
7321, <https://doi.org/10.5194/acp-14-7291-2014>, 2014.

Grosvenor, D. P., Sourdeval, O., Zuidema, P., Ackerman, A., Alexandrov, M. D., Bennartz, R.,  
Boers, R., Cairns, B., Chiu, J. C., Christensen, M., Deneke, H., Diamond, M., Feingold, G.,  
Fridlind, A., Hünerbein, A., Knist, C., Kollias, P., Marshak, A., McCoy, D., Merk, D.,  
885 Painemal, D., Rausch, J., Rosenfeld, D., Russchenberg, H., Seifert, P., Sinclair, K., Stier, P.,  
van Diedenhoven, B., Wendisch, M., Werner, F., Wood, R., Zhang, Z., and Quaas, J.:  
Remote Sensing of Droplet Number Concentration in Warm Clouds: A Review of the  
Current State of Knowledge and Perspectives, *Rev. Geophys.*, 56, 409–  
453, <https://doi.org/10.1029/2017RG000593>, 2018.

890 Gryspeerd, E., McCoy, D. T., Crosbie, E., Moore, R. H., Nott, G. J., Painemal, D., Small-Griswold,  
J., Sorooshian, A., and Ziemba, L.: The impact of sampling strategy on the cloud droplet



- number concentration estimated from satellite data, *Atmos. Meas. Tech. Discuss.* [preprint], <https://doi.org/10.5194/amt-2021-371>, in review, 2021.
- Gryspeerd, E., Mülmenstädt, J., Gettelman, A., Malavelle, F. F., Morrison, H., Neubauer, D.,  
895 Partridge, D. G., Stier, P., Takemura, T., Wang, H., Wang, M., and Zhang, K.: Surprising similarities in model and observational aerosol radiative forcing estimates, *Atmos. Chem. Phys.*, 20, 613–623, <https://doi.org/10.5194/acp-20-613-2020>, 2020.
- Gupta, S., McFarquhar, G. M., O'Brien, J. R., Delene, D. J., Poellot, M. R., Dobracki, A., Podolske, J. R., Redemann, J., LeBlanc, S. E., Segal-Rozenhaimer, M., and Pistone, K.: Impact of the  
900 variability in vertical separation between biomass burning aerosols and marine stratocumulus on cloud microphysical properties over the Southeast Atlantic, *Atmos. Chem. Phys.*, 21, 4615–4635, <https://doi.org/10.5194/acp-21-4615-2021>, 2021.
- Gupta, S., McFarquhar, G. M., O'Brien, J. R., Poellot, M. R., Delene, D. J., Miller, R. M., and Small  
905 Griswold, J. D.: Factors affecting precipitation formation and precipitation susceptibility of marine stratocumulus with variable above- and below-cloud aerosol concentrations over the Southeast Atlantic, *Atmos. Chem. Phys.*, 22, 2769–2793, <https://doi.org/10.5194/acp-22-2769-2022>, 2022.
- Hansen, J. and Travis, L. D.: Light scattering in planetary atmospheres, *Space Sci. Rev.*, 16, 527–610, 1974.
- 910 Hartmann, D. L., Ockert-Bell, M. E., and Michelsen, M. L.: The effect of cloud type on Earth's energy balance: Global analysis, *J. Climate*, 5, 1281–1304, 1992.
- Haywood, J. M., Abel, S. J., Barrett, P. A., Bellouin, N., Blyth, A., Bower, K. N., Brooks, M., Carslaw, K., Che, H., Coe, H., Cotterell, M. I., Crawford, I., Cui, Z., Davies, N., Dingley, B., Field, P.,



- Formenti, P., Gordon, H., de Graaf, M., Herbert, R., Johnson, B., Jones, A. C., Langridge, J.  
915 M., Malavelle, F., Partridge, D. G., Peers, F., Redemann, J., Stier, P., Szpek, K., Taylor, J. W.,  
Watson-Parris, D., Wood, R., Wu, H., and Zuidema, P.: The CLOUD–Aerosol–Radiation  
Interaction and Forcing: Year 2017 (CLARIFY-2017) measurement campaign, *Atmos.*  
*Chem. Phys.*, 21, 1049–1084, <https://doi.org/10.5194/acp-21-1049-2021>, 2021.
- Haywood, J. M., Osborne, S. R., and Abel, S. J.: The effect of overlying absorbing aerosol layers on  
920 remote sensing retrievals of cloud effective radius and cloud optical depth, *Q. J. R.*  
*Meteorol. Soc.*, 130, 779–800, 2004.
- Janssen, R. H. H., Ganzeveld, L. N., Kabat, P., Kulmala, M., Nieminen, T., and Roebeling, R. A.:  
Estimating seasonal variations in cloud droplet number concentration over the boreal  
forest from satellite observations, *Atmos. Chem. Phys.*, 11, 7701–7713,  
925 <https://doi.org/10.5194/acp-11-7701-2011>, 2011.
- Johnson, B. T., Shine, K. P., and Forster, P. M.: The semi-direct aerosol effect: Impact of absorbing  
aerosols on marine stratocumulus, *Q. J. Roy. Meteor. Soc.*, 130, 1407–1422, 2004.
- King, M. D., Tsay, S. C., Platnick, S., Wang, M., & Liou, K. N. (1998). Cloud retrieval algorithms for  
MODIS: Optical thickness, effective particle radius, and thermodynamic phase. In  
930 *Algorithm Theor. Basis Doc. ATBD-MOD-05*. Greenbelt, Md: Goddard Space Flight Center.
- King, N. J., Bower, K. N., Crosier, J., and Crawford, I.: Evaluating MODIS cloud retrievals with in  
situ observations from VOCALS-REx, *Atmos. Chem. Phys.*, 13, 191–209,  
<https://doi.org/10.5194/acp-13-191-2013>, 2013.



- King, W. D., Parkin, D. A., and Handsworth, R. J.: A hot-wire liquid water device having fully  
935 calculable response characteristics, *J. Appl. Meteorol.*, 17, 1809–1813,  
[https://doi.org/10.1175/1520-0450\(1978\)017<1809:AHWLWD>2.0.CO;2](https://doi.org/10.1175/1520-0450(1978)017<1809:AHWLWD>2.0.CO;2), 1978.
- Lance, S., Brock, C. A., Rogers, D., and Gordon, J. A.: Water droplet calibration of the Cloud  
Droplet Probe (CDP) and in-flight performance in liquid, ice and mixed-phase clouds  
during ARCPAC, *Atmos. Meas. Tech.*, 3, 1683–1706, [https://doi.org/10.5194/amt-3-1683-](https://doi.org/10.5194/amt-3-1683-2010)  
940 2010, 2010.
- Lance, S.: Coincidence Errors in a Cloud Droplet Probe (CDP) and a Cloud and Aerosol  
Spectrometer (CAS), and the Improved Performance of a Modified CDP, *J. Atmos. Ocean.  
Tech.*, 29, 1532–1541, doi:10.1175/JTECH-D-11-00208.1, 2012.
- Lawson, R. P., Stewart, R. E., and Angus, L. J.: Observations and numerical simulations of the origin  
945 and development of very large snowflakes, *J. Atmos. Sci.*, 55, 3209–3229, 1998.
- Lawson, R. P., O’Connor, D., Zmarzly, P., Weaver, K., Baker, B. A., Mo, Q., and Jonsson, H.: The 2D-  
S (Stereo) probe: Design and preliminary tests of a new airborne, high-speed, high-  
resolution imaging probe, *J. Atmos. Ocean. Tech.*, 23, 1462–1477, 2006.
- Lenhardt, E.: Relationships Between Lidar Aerosol Extinction and Backscatter Coefficients with  
950 CCN Number Concentrations in the Southeast Atlantic, OU – Theses [1749],  
<https://hdl.handle.net/11244/330151>, 2021.
- Loeb, N. G., Wielicki, B. A., Doelling, D. R., Smith, G. L., Keyes, D. F., Kato, S., Manalo-Smith, N.,  
and Wong, T.: Toward optimal closure of the Earth’s Top-of-Atmosphere radiation  
budget, *J. Climate*, 22, 3, 748–766, <https://doi.org/10.1175/2008JCLI2637.1>, 2009.



- 955 Mallet, M., Nabat, P., Johnson, B., Michou, M., Haywood, J. M., Chen, C., Dubovik, O.: Climate models generally underrepresent the warming by Central Africa biomass-burning aerosols over the Southeast Atlantic. *Sci. Adv.*, 7, eabg9998, 2021.
- Martin, G. M., Johnson, D. W., and Spice, A.: The measurement and parameterization of effective radius of droplets in warm stratocumulus clouds, *J. Atmos. Sci.*, 51, 1823–1842, 1994.
- 960 McComiskey, A. and Feingold, G.: The scale problem in quantifying aerosol indirect effects, *Atmos. Chem. Phys.*, 12, 1031–1049, <https://doi.org/10.5194/acp-12-1031-2012>, 2012.
- McFarquhar, G. M. and Heymsfield, A. J. : The definition and significance of an effective radius for ice clouds, *J. Atmos. Sci.*, 55, 2039–2052, 1998.
- McFarquhar, G. M. and Heymsfield, A. J.: Parameterizations of INDOEX microphysical
- 965 measurements and calculations of cloud susceptibility: Applications for climate studies, *J. Geophys. Res.*, 106, 28675–28698, 2001.
- McFarquhar, G. M. and Wang, H.: Effects of Aerosols on Trade Wind Cumuli over the Indian Ocean: Model Simulations, *Q. J. R. Meteor. Soc.*, 132, 821–843, 2006.
- McFarquhar, G. M., Finlon, J. A., Stechman, D. M., Wu, W., Jackson, R. C., and Freer, M.: University
- 970 of Illinois/Oklahoma Optical Array Probe (OAP) Processing Software, <https://doi.org/10.5281/zenodo.1285969>, 2018.
- Merk, D., Deneke, H., Pospichal, B., and Seifert, P.: Investigation of the adiabatic assumption for estimating cloud micro- and macrophysical properties from satellite and ground observations, *Atmos. Chem. Phys.*, 16, 933–952, [https://doi.org/10.5194/acp-16-933-](https://doi.org/10.5194/acp-16-933-2016)
- 975 2016, 2016.





- Meyer, K., Platnick, S., and Zhang, Z.: Simultaneously inferring above-cloud absorbing aerosol optical thickness and underlying liquid phase cloud optical and microphysical properties using MODIS, *J. Geophys. Res.-Atmos.*, 120, 5524–5547, doi:10.1002/2015JD023128, 2015.
- 980 Min, Q., Joseph, E., Lin, Y., Min, L., Yin, B., Daum, P. H., Kleinman, L. I., Wang, J., and Lee, Y.-N.: Comparison of MODIS cloud microphysical properties with in-situ measurements over the Southeast Pacific, *Atmos. Chem. Phys.*, 12, 11261–11273, <https://doi.org/10.5194/acp-12-11261-2012>, 2012.
- Myhre, G., Shindell, D., Bréon, F.-M., Collins, W., Fuglestvedt, J., Huang, J., Koch, D., Lamarque, 985 J.-F., Lee, D., Mendoza, B., Nakajima, T., Robock, A., Stephens, G., Takemura, T. and Zhang, H.: Anthropogenic and Natural Radiative Forc-ing. In: *Climate Change 2013: The Physical Science Basis. Contribution of Working Group I to the Fifth Assessment Report of the Intergovernmental Panel on Climate Change*, edited by: Stocker, T. F., Qin, D., Plattner, G.-K., Tignor, M., Allen, S. K., Boschung, J., Nauels, A., Xia, Y., Bex, V., and Midgley, P. M., 990 Cambridge University Press, 571–657, 2013.
- Nakajima, T. and King, M. D.: Determination of the optical thickness and effective particle radius of clouds from reflected solar radiation measurements. Part I: Theory, *J. Atmos. Sci.*, 47, 1878– 1893, 1990.
- Nakajima, T.Y., Suzuki, K., and Stephens, G.L.: Droplet growth in warm water clouds observed by 995 the A-Train. Part I: Sensitivity analysis of the MODIS-derived cloud droplet sizes. *Journal of the Atmospheric Sciences*, 67(6), pp.1884-1896, 2010.



Noble, S. R., and Hudson, J. G.: MODIS comparisons with northeastern Pacific in situ stratocumulus microphysics, *J. Geophys. Res. Atmos.*, 120, 8332–8344, doi:10.1002/2014JD022785, 2015.

1000 ORACLES Science Team: Suite of Aerosol, Cloud, and Related Data Acquired Aboard P3 During ORACLES 2018, Version 2, NASA Ames Earth Science Project Office, [https://doi.org/10.5067/Suborbital/ORACLES/P3/2018\\_V2](https://doi.org/10.5067/Suborbital/ORACLES/P3/2018_V2), 2020a.

ORACLES Science Team: Suite of Aerosol, Cloud, and Related Data Acquired Aboard P3 During ORACLES 2017, Version 2, NASA Ames Earth Science Project Office,  
1005 [https://doi.org/10.5067/Suborbital/ORACLES/P3/2017\\_V2](https://doi.org/10.5067/Suborbital/ORACLES/P3/2017_V2), 2020b.

ORACLES Science Team: Suite of Aerosol, Cloud, and Related Data Acquired Aboard P3 During ORACLES 2016, Version 2, NASA Ames Earth Science Project Office,  
[https://doi.org/10.5067/Suborbital/ORACLES/P3/2016\\_V2](https://doi.org/10.5067/Suborbital/ORACLES/P3/2016_V2), 2020c.

Painemal, D. and Zuidema, P.: Assessment of MODIS cloud effective radius and optical thickness  
1010 retrievals over the Southeast Pacific with VOCALS-REx in situ measurements, *J. Geophys. Res.-Atmos.*, 116, D24206, doi:10.1029/2011JD016155, 2011.

Painemal, D., Chang, F.-L., Ferrare, R., Burton, S., Li, Z., Smith Jr., W. L., Minnis, P., Feng, Y., and Clayton, M.: Reducing uncertainties in satellite estimates of aerosol–cloud interactions over the subtropical ocean by integrating vertically resolved aerosol observations, *Atmos. Chem. Phys.*, 20, 7167–7177, <https://doi.org/10.5194/acp-20-7167-2020>, 2020.  
1015

Painemal, D., Spangenberg, D., Smith Jr., W. L., Minnis, P., Cairns, B., Moore, R. H., Crosbie, E., Robinson, C., Thornhill, K. L., Winstead, E. L., and Ziemba, L.: Evaluation of satellite retrievals of liquid clouds from the GOES-13 imager and MODIS over the midlatitude



1020 North Atlantic during the NAAMES campaign, *Atmos. Meas. Tech.*, 14, 6633–6646,  
<https://doi.org/10.5194/amt-14-6633-2021>, 2021.

Platnick, S. (2000). Vertical photon transport in cloud remote sensing problems. *Journal of Geophysical Research*, 105(D18), 22,919–22,935. <https://doi.org/10.1029/2000JD900333>

1025 Platnick, S., King, M. D., Ackerman, S. A., Menzel, W. P., Baum, B. A., Riedi, J. C., & Frey, R. A.,  
2003: The MODIS cloud products: Algorithms and examples from Terra. *IEEE Transactions on Geoscience and Remote Sensing*, 41(2), 459–473.  
<https://doi.org/10.1109/tgrs.2002.808301>.

Platnick, S. and Twomey, S.: Determining the susceptibility of cloud albedo to changes in droplet concentration with the advanced very high resolution radiometer, *J. Appl. Meteor.*, 33, 334–346, 1994.

1030 Platnick, S., K. G. Meyer, M. D. King, G. Wind, N. Amarasinghe, B. Marchant, G. T. Arnold, Z. Zhang, P. A. Hubanks, R. E. Holz, P. Yang, W. L. Ridgway, and J. Riedi: The MODIS cloud optical and microphysical products: Collection 6 updates and examples from Terra and Aqua. *IEEE Trans. Geosci. Remote Sens.*, 55, 502–525, 2017b.

1035 Platnick, S., S. Ackerman, M. King, G. Wind, K. Meyer, P. Menzel, R. Frey, R. Holz, B. Baum, and P. Yang: MODIS atmosphere L2 cloud product (O6\_L2), NASA MODIS Adaptive Processing System, Goddard Space Flight Center, [doi:10.5067/MODIS/MOD06\_L2.061; doi:10.5067/MODIS/MYD06\_L2.061], 2017a.

1040 Peers, F., Francis, P., Abel, S. J., Barrett, P. A., Bower, K. N., Cotterell, M. I., Crawford, I., Davies, N. W., Fox, C., Fox, S., Langridge, J. M., Meyer, K. G., Platnick, S. E., Szpek, K., and Haywood, J. M.: Observation of absorbing aerosols above clouds over the south-east



- Atlantic Ocean from the geostationary satellite SEVIRI – Part 2: Comparison with MODIS and aircraft measurements from the CLARIFY-2017 field campaign, *Atmos. Chem. Phys.*, 21, 3235–3254, <https://doi.org/10.5194/acp-21-3235-2021>, 2021.
- 1045 Quaas, J., Arola, A., Cairns, B., Christensen, M., Deneke, H., Ekman, A. M. L., Feingold, G., Fridlind, A., Gryspeerd, E., Hasekamp, O., Li, Z., Lipponen, A., Ma, P.-L., Mülmenstädt, J., Nenes, A., Penner, J. E., Rosenfeld, D., Schrödner, R., Sinclair, K., Sourdeval, O., Stier, P., Tesche, M., van Diedenhoven, B., and Wendisch, M.: Constraining the Twomey effect from satellite observations: issues and perspectives, *Atmos. Chem. Phys.*, 20, 15079–15099, <https://doi.org/10.5194/acp-20-15079-2020>, 2020.
- 1050 Rajapakshe, C., Zhang, Z., Yorks, J. E., Yu, H., Tan, Q., Meyer, K., Platnick, S., and Winker, D. M.: Seasonally transported aerosol layers over southeast Atlantic are closer to underlying clouds than previously reported, *Geophys. Res. Lett.*, 44, 5818–5825, <https://doi.org/10.1002/2017GL073559>, 2017.
- 1055 Rausch, J., Meyer, K., Bennartz, R., and Platnick, S.: Differences in liquid cloud droplet effective radius and number concentration estimates between MODIS collections 5.1 and 6 over global oceans, *Atmos. Meas. Tech.*, 10, 2105–2116, <https://doi.org/10.5194/amt-10-2105-2017>, 2017.
- 1060 Redemann, J., Wood, R., Zuidema, P., Doherty, S. J., Luna, B., LeBlanc, S. E., Diamond, M. S., Shinozuka, Y., Chang, I. Y., Ueyama, R., Pfister, L., Ryoo, J.-M., Dobracki, A. N., da Silva, A. M., Longo, K. M., Kacenelenbogen, M. S., Flynn, C. J., Pistone, K., Knox, N. M., Piketh, S. J., Haywood, J. M., Formenti, P., Mallet, M., Stier, P., Ackerman, A. S., Bauer, S. E., Fridlind, A. M., Carmichael, G. R., Saide, P. E., Ferrada, G. A., Howell, S. G., Freitag, S., Cairns, B.,



- 1065 Holben, B. N., Knobelspiesse, K. D., Tanelli, S., L'Ecuyer, T. S., Dzambo, A. M., Sy, O. O.,  
McFarquhar, G. M., Poellot, M. R., Gupta, S., O'Brien, J. R., Nenes, A., Kacarab, M., Wong,  
J. P. S., Small-Griswold, J. D., Thornhill, K. L., Noone, D., Podolske, J. R., Schmidt, K. S.,  
Pilewskie, P., Chen, H., Cochrane, S. P., Sedlacek, A. J., Lang, T. J., Stith, E., Segal-  
Rozenhaimer, M., Ferrare, R. A., Burton, S. P., Hostetler, C. A., Diner, D. J., Seidel, F. C.,  
Platnick, S. E., Myers, J. S., Meyer, K. G., Spangenberg, D. A., Maring, H., and Gao, L.: An  
overview of the ORACLES (ObseRvations of Aerosols above CLouds and their intEractionS)  
1070 project: aerosol–cloud–radiation interactions in the southeast Atlantic basin, *Atmos.*  
*Chem. Phys.*, 21, 1507–1563, <https://doi.org/10.5194/acp-21-1507-2021>, 2021.
- Sinclair, K., van Dierenhoven, B., Cairns, B., Alexandrov, M., Dzambo, A. M., & L'Ecuyer, T.:  
Inference of precipitation in warm stratiform clouds using remotely sensed observations  
of the cloud top droplet size distribution, *Geophysical Research Letters*, 48,  
1075 e2021GL092547. <https://doi.org/10.1029/2021GL092547>, 2021.
- Slingo, A.: Sensitivity of the Earth's radiation budget to changes in low clouds, *Nature*, 343, 49–  
51, <https://doi.org/10.1038/343049a0>, 1990.
- Szczodrak, M., Austin, P. H., and Krummel, P. B.: Variability of Optical Depth and Effective Radius  
in Marine Stratocumulus Clouds, *J. Atmos. Sci.*, 58, 2912–  
1080 2926, [https://doi.org/10.1175/1520-0469\(2001\)058<2912:VOODAE>2.0.CO;2](https://doi.org/10.1175/1520-0469(2001)058<2912:VOODAE>2.0.CO;2), 2001.
- Thornhill, K. L., Anderson, B. E., Barrick, J. D. W., Bagwell, D. R., Friesen, R., and Lenschow, D.: Air  
motion inter-comparison flights during Transport and Chemical Evolution in the Pacific  
(TRACE-P)/ACE-ASIA, *J. Geophys. Res.*, 108, <https://doi.org/10.1029/2002JD003108>,  
2003.



- 1085 Twomey, S.: Pollution and the Planetary Albedo, *Atmos. Environ.*, 8, 1251–1256, 1974.
- Twomey, S.: The influence of pollution on the shortwave albedo of clouds. *J. Atmos. Sci.*, 34, 1149–1152, 1977.
- Wilcox, E. M.: Stratocumulus cloud thickening beneath layers of absorbing smoke aerosol, *Atmos. Chem. Phys.*, 10, 11769–11777, <https://doi.org/10.5194/acp-10-11769-2010>, 2010.
- 1090 Witte, M. K., Yuan, T., Chuang, P. Y., Platnick, S., Meyer, K. G., Wind, G., & Jonsson, H. H.: MODIS retrievals of cloud effective radius in marine stratocumulus exhibit no significant bias. *Geophysical Research Letters*, 45, 10,656–10,664. <https://doi.org/10.1029/2018GL079325>, 2018.
- Wood, R.: Stratocumulus Clouds, *Mon. Weather Rev.*, 140, 2373–2423, doi:10.1175/MWR-D-11-1095 00121.1, 2012.
- Wood, R. and Hartmann, D. L.: Spatial variability of liquid water path in marine low cloud: the importance of mesoscale cellular convection, *J. Climate*, 19, 1748–1764, 2006.
- Zeng, S., Riedi, J., Trepte, C. R., Winker, D. M., and Hu, Y.-X.: Study of global cloud droplet number concentration with A-Train satellites, *Atmos. Chem. Phys.*, 14, 7125–7134, <https://doi.org/10.5194/acp-14-7125-2014>, 2014.
- 1100 Zhang, Z. and Platnick, S.: An assessment of differences between cloud effective particle radius retrievals for marine water clouds from three MODIS spectral bands, *J. Geophys. Res.-Atmos.*, 116, D20215, doi:10.1029/2011JD016216, 2011.
- Zinner, T., Wind, G., Platnick, S., and Ackerman, A. S.: Testing remote sensing on artificial 1105 observations: impact of drizzle and 3-D cloud structure on effective radius retrievals, *Atmos. Chem. Phys.*, 10, 9535–9549, <https://doi.org/10.5194/acp-10-9535-2010>, 2010.



Zuidema, P., Redemann, J., Haywood, J., Wood, R., Piketh, S., Hipondoka, M. and Formenti, P.:

Smoke and Clouds above the Southeast Atlantic: Upcoming Field Campaigns Probe

Absorbing Aerosol's Impact on Climate, Bull. Am. Meteorol. Soc., 160129100143006,

1110

doi:10.1175/BAMS-D-15-00082.1, 2016.